



HAL
open science

Controls on the magmatic fraction of extension at mid-ocean ridges

Jean-Arthur Olive, Pierre Dublanchet

► **To cite this version:**

Jean-Arthur Olive, Pierre Dublanchet. Controls on the magmatic fraction of extension at mid-ocean ridges. *Earth and Planetary Science Letters*, 2020, 549, pp.116541. 10.1016/j.epsl.2020.116541 . hal-02921482

HAL Id: hal-02921482

<https://hal.science/hal-02921482>

Submitted on 25 Aug 2020

HAL is a multi-disciplinary open access archive for the deposit and dissemination of scientific research documents, whether they are published or not. The documents may come from teaching and research institutions in France or abroad, or from public or private research centers.

L'archive ouverte pluridisciplinaire **HAL**, est destinée au dépôt et à la diffusion de documents scientifiques de niveau recherche, publiés ou non, émanant des établissements d'enseignement et de recherche français ou étrangers, des laboratoires publics ou privés.

1 **Controls on the magmatic fraction of extension at mid-ocean ridges**

2 Jean-Arthur Olive^{1*} and Pierre Dublanquet²

3 ¹*Laboratoire de Géologie, Ecole Normale Supérieure / CNRS UMR 8538, PSL Research*
4 *University, Paris 75005, France.*

5 ²*MINES ParisTech, PSL Research University, Centre de Géosciences, Fontainebleau 77305,*
6 *France.*

7 **Corresponding author: olive@geologie.ens.fr*

8

9

10

11 **Keywords**

12 Mid-ocean ridge; seafloor spreading; normal faults; diking; submarine volcanism.

13

14

15

16 **Highlights**

17 • Magmatic component of seafloor spreading (M) increases non-linearly with spreading rate.

18 • Stress interactions between fault slip events and magma intrusions provide physical basis for
19 M .

20 • Axial lithosphere thickness and rate of pressure build-up in sills are primary controls on M .

21 • Transitions between modes of seafloor spreading reflect thresholds in axial lithosphere
22 thickness.

23 **Abstract**

24 The fraction M of plate separation accommodated by magma emplacement at mid-ocean ridges
25 has been recognized as the main control on seafloor spreading modes, yet the factors that control
26 M itself are poorly understood. Here we put forward a simple theoretical framework explaining
27 M in terms of short-term cycles of earthquakes and dike intrusions interacting with one another
28 by modulating the stress state of the ridge axis. Axial lithospheric thickness and the rate of
29 pressure build-up in shallow, replenishing magma sills are the two main parameters controlling
30 M in our simulations. Combined with plausible scenarios for the increase of pressure build-up
31 rate and the decrease of lithospheric thickness with increasing spreading rate, our model
32 appropriately brackets available measurements of M from slow, intermediate, and fast-spreading
33 ridges. Our model further suggests that the transitions between major modes of seafloor
34 spreading (detachment faulting, symmetric faulting, and fully-magmatic) correspond to
35 thresholds in axial lithospheric thickness, and that the great variability in M at slow and ultraslow
36 ridges directly reflects along-axis variability in thermal structure. More generally, this implies
37 that the balance between bottom-up magmatic heating and top-down hydrothermal cooling fully
38 determines the time-averaged rate of magmatic intrusions in the brittle lithosphere, and thus the
39 modes of mid-ocean ridge faulting which shape $\sim 2/3$ of Earth's surface.

40

41 **1. Introduction**

42 Seafloor spreading at mid-ocean ridges (MORs) typically involves a combination of tectonic
43 and magmatic processes. Adiabatic decompression melting in the asthenosphere produces
44 magma, which ascends to the ridge axis and crystallizes in sills, dikes or lava flows, forming new
45 oceanic crust. Magmatic emplacement is accompanied by normal faulting, which dissects the

46 brittle upper crust into discrete blocks that undergo uplift and tilting as they are advected off-axis
47 (MacDonald et al., 1996). These processes interact over geological time to shape elongated,
48 regularly spaced abyssal hills: the most common landform on the surface of the Earth (e.g.,
49 Kappel and Ryan, 1986).

50 The long-term (>100 kyr) partitioning of tectonic and magmatic extension at MORs is
51 straightforwardly quantified by summing the heaves of normal faults located within a certain
52 distance to the axis (e.g., Escartín et al., 1999; Schouten et al., 2010). The ratio of magmatically
53 accommodated extension to total plate separation —commonly referred to as M (**Fig. 1a**)—
54 exceeds ~ 0.9 at fast-spreading ridges (full spreading rate $U \geq 8$ cm/yr) such as the East Pacific
55 Rise (Cowie et al., 1993; Buck et al., 2005; Escartín et al., 2007). At intermediate-spreading
56 MORs ($5 \leq U < 8$ cm/yr), M typically ranges between ~ 0.7 and ~ 0.95 (Ito and Behn, 2008),
57 although values in excess of 0.95 have recently been reported locally along the Chile Ridge and
58 the Southeast Indian Ridge (Howell et al., 2016). Variability in the M fraction is maximized at
59 slow ($1.5 \leq U < 5$ cm/yr) and ultraslow ($U < 1.5$ cm/yr) MORs. These ridges are characterized by
60 the along-axis juxtaposition of sections with symmetrically faulted (staircase-like) topography,
61 and sections populated by large-offset detachment faults shaping oceanic core complexes and
62 other irregular bathymetric highs (Escartín et al., 2008; Sauter et al., 2011). M ranges between
63 ~ 0.6 and ~ 0.8 at symmetrically faulted sections of the Mid-Atlantic ridge (Cowie et al., 1993; Ito
64 and Behn, 2008; Olive and Escartín, 2016). At detachment-bearing sections of the Mid-Atlantic
65 Ridge, M typically varies between ~ 0.2 and ~ 0.6 (Behn and Ito, 2008; MacLeod et al., 2009;
66 Schouten et al., 2010). It can reach zero in amagmatic sections of the ultraslow Southwest Indian
67 Ridge, where the seafloor consists of serpentinized peridotite exhumed by detachment faults
68 (Dick et al., 2003; Sauter et al., 2011; Cannat et al., 2019).

69 Mechanical models suggest that M is the primary control on MOR tectonics (Buck et al.,
70 2005). This includes the average spacing and maximum offset of normal faults, the presence of
71 an axial valley vs. an axial high, and the development of symmetric faults vs. detachments (Behn
72 and Ito, 2008; Ito and Behn, 2008; Tucholke et al., 2008; Olive et al., 2010; 2015; Tian and Choi,
73 2017; Liu and Buck, 2018; 2020; Howell et al., 2019). The primary effect of the M parameter is
74 to modulate the rate at which an active fault formed in thin axial lithosphere will migrate off-
75 axis, encountering progressively thicker and stronger lithosphere. At some point, breaking a new
76 fault in thin axial lithosphere becomes more energetically favorable than continuing to slip on a
77 fault that has moved off-axis. The greater the M , the sooner this point is reached, meaning that
78 faults form in closer succession on either side of the axis, and accumulate less total slip. This
79 leads to regularly spaced, symmetric abyssal hills. When M is close to 0.5, faults can remain at
80 the ridge axis for extended periods of time and accumulate very large offsets, making
81 detachment faulting possible (Buck et al., 2005). Values of $M < 0.5$ enable faults to migrate
82 towards the axis, which in numerical models results in complex inward- and outward-dipping
83 faults that cross-cut each other (Tucholke et al., 2008; Olive et al., 2010; Bickert et al., 2020).

84 A common limitation of all the models listed above is that they treat M as an empirical input
85 parameter that cannot be determined from other observables that characterize MOR axes.
86 Measurements show that M increases non-linearly with spreading rate (Olive et al., 2015) in a
87 manner that resembles the increase in magma flux ($\Phi_C = H_C \times U$, with H_C the thickness of the
88 magmatic crust) from ultraslow to fast MOR (e.g., Cannat et al., 2008) (**Fig. 1a**). Even though
89 the M parameter is often used interchangeably with "magma supply", it has never been
90 quantitatively related to Φ_C , let alone spreading rate. It is also important to note that M only
91 refers to magma intruded in the brittle lithosphere, and ignores melt emplaced in the ductile

92 portion of the ridge axis, which Olive et al. (2010) argued does not impact fault evolution. One
93 might further expect that the strength and thickness of axial lithosphere should affect the modes
94 of shallow melt emplacement, and therefore the M value (e.g., Keller et al., 2013).

95 Here we propose a quantitative framework that identifies first-order controls on M , and
96 explains its non-linear increase with spreading rate (**Fig. 1a**). Our approach is rooted in the fact
97 that on human time scales, seafloor spreading primarily manifests as normal faulting
98 earthquakes, which can reach magnitudes up to ~ 6.5 (e.g., Solomon et al., 1988; Cowie et al.,
99 1993; Olive and Escartín, 2016), as well as dike intrusion events that are typically ~ 1 -m wide
100 and sometimes lead to a seafloor eruption (e.g., Qin and Buck, 2008; Tan et al., 2016). We
101 design the simplest possible analytical model of tectono-volcanic cycles, in which plate
102 separation on decadal time scales is either taken up by a dike or an increment of fault slip,
103 depending on the ever-evolving thresholds for magmatic intrusion and fault slip. Averaging the
104 model behavior over many cycles yields an effective M value that reflects the influence of
105 spreading rate, lithospheric thickness and melt flux to the ridge axis.

106

107 **2. A simple model of tectono-magmatic interactions**

108 2.1. Governing equations

109 We consider an idealized mid-ocean ridge axis (**Fig. 1b**) subjected to a full plate separation rate
110 U , which deforms over a characteristic cross-axis length scale $L \sim 10$ km. The brittle on-axis
111 lithosphere has a thickness H and overlies a sill-like axial melt lens (AML) located immediately
112 below the brittle-ductile transition. Horizontal stresses at the axis (at depth z below seafloor)
113 consist of a lithostatic component partially relieved by pore pressure, and a horizontal tectonic
114 component $\Delta\sigma_{xx}$ such that

115
$$\sigma_{xx}(z, t) = -\rho g(1 - \lambda)z + \Delta\sigma_{xx}(t), \quad (1)$$

116 where ρ is the density of the crust (2900 kg/m³), and g is the acceleration of gravity (9.8 m/s²). λ
 117 denotes fluid pressure normalized by lithostatic pressure $\rho g z$ and will be assumed hydrostatic,
 118 i.e., $\lambda = \rho_w / \rho = 0.34$ (with ρ_w the density of water) except near the roof of the AML where
 119 $\lambda = 0$. The horizontal tectonic stress (positive in tension) is assumed to continuously increase
 120 over time at a rate prescribed by the far-field plate separation rate:

121
$$\frac{\partial \Delta\sigma_{xx}}{\partial t} = \frac{EU}{L}, \quad (2)$$

122 where E is the Young's modulus of axial lithosphere. A plausible range for E is 5–30 GPa (Heap
 123 et al., 2020). In the following we will use $E = 10$ GPa unless otherwise specified, and a Poisson's
 124 ratio $\nu = 0.25$. $\Delta\sigma_{xx}$ however cannot increase to infinity and can reach either a tectonic threshold
 125 $\Delta\sigma_{xx}^F$, which triggers a seismic (or aseismic) slip event on a fault, or a magmatic threshold $\Delta\sigma_{xx}^M$,
 126 which triggers the intrusion of a vertical dike.

127 The tectonic threshold is determined by assuming the ridge axis is bounded by an
 128 optimally-oriented, cohesionless normal fault of friction coefficient $\mu = 0.6$. The static strength
 129 of the fault is thus reached when

130
$$\Delta\sigma_{xx}(t = t_F) = \Delta\sigma_{xx}^F = \frac{\mu\rho g(1-\lambda)H}{\mu + \sqrt{1+\mu^2}}. \quad (3)$$

131 Equation (3) corresponds to the strength of the fault averaged over the thickness of the brittle
 132 lithosphere (e.g., Behn and Ito, 2008). For simplicity, we assume that a tectonic event occurring
 133 at time t_F corresponds to an increment in fault slip δ_F in the horizontal direction (e.g., $\delta_F = 1$ m
 134 for a magnitude ~ 6 earthquake with a standard stress drop of ~ 1 MPa). Such events induce
 135 compression at the axis, which instantaneously relieves a small portion of the built-up horizontal

136 tectonic stress. We model this effect by subtracting a stress increment from $\Delta\sigma_{xx}$ after each
 137 event:

$$138 \quad \Delta\sigma_{xx}(t = t_F^+) = \Delta\sigma_{xx}(t = t_F^-) - E \frac{\delta_F}{L}. \quad (4)$$

139 At certain times, the total horizontal stress at the base of the brittle lithosphere may reach the
 140 rocks' tensile strength T_0 (~ 1 MPa), triggering the intrusion of a dike of width $\delta_F = 1$ m
 141 (Kelemen and Aharonov, 1998; Qin and Buck, 2008). This is because magmatic overpressure p_M
 142 in the AML (or a sill-like region within the AML) imparts an increase in total horizontal stress
 143 near the edges of the area undergoing replenishment and pressurization (Wilcock et al., 2009).
 144 This is illustrated in Supplementary Figure S1. The additional tensile stress above the sill is
 145 proportional to magmatic overpressure, and may be exacerbated by stress concentrations around
 146 sharp edges or irregularities along the top of the AML. The zero-dimensional nature of our
 147 approach prevents us from incorporating these effects in a systematic manner. We therefore
 148 assume that the increase in horizontal tension near a pressurized sill is equal to magmatic
 149 overpressure and thus fluctuates at a rate imposed by the dynamics of magmatic replenishment.
 150 The area above the AML is known to be impermeable to fluid circulation (Gillis 2008). It
 151 therefore experiences a confining pressure equal to $p_w + \rho gH$, where p_w is water pressure at the
 152 seafloor (19.6 MPa for 2000 m depth). With these assumptions, the threshold for diking can be
 153 expressed as

$$154 \quad -p_w - \rho gH + \Delta\sigma_{xx} + p_M = T_0, \quad (5)$$

155 which can be recast as:

$$156 \quad \Delta\sigma_{xx}(t = t_M) = \Delta\sigma_{xx}^M(t = t_M) = T_0 - p_M(t = t_M) + p_w + \rho gH. \quad (6)$$

157 When the threshold described by equation (6) is reached at time t_M , the instantaneous
 158 emplacement of a dike imparts an increment of compression on the axis, which we model as:

159
$$\Delta\sigma_{xx}(t = t_M^+) = \Delta\sigma_{xx}(t = t_M^-) - E \frac{\delta_M}{L}. \quad (7)$$

160 Equation (6) shows that the diking threshold decreases through time as magma overpressure
 161 builds up. We assume that this occurs at a constant rate \dot{p}_M , which depends on the volume flux of
 162 magma that continuously replenishes the AML. As the intrusion of a dike temporarily connects
 163 the AML to the seafloor, it likely lowers magma pressure to a static state, meaning that magmatic
 164 overpressure drops to zero following a diking event:

165
$$p_M(t = t_M^+) = 0. \quad (8)$$

166 When this occurs, the magma intrusion threshold is maximized:

167
$$\Delta\sigma_{xx}^{M,MAX} = T_0 + p_w + \rho gH. \quad (9)$$

168 Finally, we assume that slip events on ridge-bounding faults, which relax the built-up axial stress
 169 $\Delta\sigma_{xx}$, do not otherwise influence the ever-changing threshold for dike initiation $\Delta\sigma_{xx}^M(t)$.

170

171 2.2. Choice of parameter values

172 2.2.1. Axial lithospheric thickness

173 The thickness of axial lithosphere is a critical parameter in our model. It corresponds to the depth
 174 of the brittle-ductile transition, where the shallowest melts can pool, and below which no
 175 seismicity occurs. At sections of MORs that are magmatically robust enough for melt to be
 176 seismically imaged, the depth to the shallowest AML reflector (circles in **Fig. 2a**) constitutes a
 177 good proxy for the base of the brittle lithosphere (Sinton and Detrick, 1992; Phipps-Morgan and
 178 Chen, 1993). This dataset is however very scarce at slow MORs. There, the seismogenic depth as
 179 measured from OBS-based micro-earthquake surveys (e.g., Grevemeyer et al., 2019) constitutes
 180 a reasonable estimate of H (squares in **Fig. 2a**). To fully account for the scatter in the data, we

181 empirically bracket our estimates between two end-member trends of lithospheric thickness vs.
182 spreading rate, using the mathematical form:

$$183 \quad H(U) = H_{MIN} + (H_{MAX} - H_{MIN})e^{-\frac{U}{\Delta U}}. \quad (10)$$

184 The “thinnest” and “thickest” trends (red and blue curves in **Fig. 2a**) correspond to H_{MIN} , H_{MAX} ,
185 and ΔU of 1.2 km, 6 km, 1.8 cm/yr; and 2 km, 26 km, and 2.7 cm/yr, respectively.

186

187 2.2.2. Magmatic pressure rate

188 The rate at which magma pressure increases with time in a continuously replenishing reservoir is
189 by far the most difficult parameter to constrain in our model. Indirect estimates can be obtained
190 by measuring and modeling seafloor inflation that sometimes precedes eruptions. To date, this
191 has only been achieved at Axial seamount, a volcano located on a hot-spot influenced section of
192 the Juan de Fuca ridge (Nooner and Chadwick, 2016), and at 9°50' N on the East Pacific Rise
193 (Nooner et al., 2014). We focus on the latter example, which —being more representative of a
194 typical fast MOR segment— can be extrapolated to construct a trend of \dot{p}_M with spreading rate
195 (**Fig. 2b**). Noonan et al. (2014) deployed pressure sensors along an axis-perpendicular profile to
196 measure seafloor uplift over several years. Sensors located near the axial trough uplifted at ~7
197 cm/yr while sensors located ~10 km off-axis did not exhibit resolvable vertical motion. Upon
198 fitting this deflection profile with two end-member models of magma pocket inflation (See
199 Supplementary Material), we obtain ranges of plausible pressure rates: between 1.9×10^{-1} and
200 1.9×10^3 Pa/s for a Mogi model, and between 4.0×10^{-5} and 2.3×10^{-3} Pa/s for a laccolith model
201 (**Fig. 2b**)

202 The large discrepancy between these estimates highlights the difficulty of quantifying
203 magma pressure build-up through direct observation. We therefore complement this approach

204 with an order-of-magnitude assessment of \dot{p}_M vs. spreading rate largely following the model of
 205 Aharonov and Kelemen (1998). We treat a magmatic sill as a horizontal, elliptical pressurized
 206 crack of width w , and infinite along-axis extent. The maximum thickness h of the sill is linked to
 207 magma overpressure (Rubin, 1995a) according to:

$$208 \quad h = 2(1 - \nu)(1 + \nu) \frac{\Delta P}{E} w . \quad (11)$$

209 From equation (11) we can relate the pressure rate to the flux of magma inflating the sill (Φ ,
 210 volume flux into a single sill, per unit length along axis):

$$211 \quad \Phi = \pi(1 - \nu)(1 + \nu) \frac{\dot{p}_M}{2E} w^2 . \quad (12)$$

212 The total magma flux leading to a mean crustal thickness H_C ($= 6$ km) is simply $\Phi_C = H_C U$.
 213 Assuming this flux gets equally partitioned within N magma sills, we can derive an order-of-
 214 magnitude estimate for pressure rate as a linear function of spreading rate:

$$215 \quad \dot{p}_M = \frac{2E}{\pi(1+\nu)(1-\nu)} \frac{H_C U}{N w^2} . \quad (13)$$

216 A high estimate of \dot{p}_M vs. U can be obtained using a high estimate of E (30 GPa, Heap et al.,
 217 2020) and low estimates for w (50 m) and N (10) (Aharonov and Kelemen, 1998). Conversely, E
 218 $= 5$ GPa, $w = 500$ m (Wilcock et al., 2009), and $N = 100$ provide a low estimate of \dot{p}_M . A
 219 geometric average of these two end-members yields a reasonable intermediate estimate of
 220 $\partial \dot{p}_M / \partial U = 6.312 \times 10^7$ Pa.m⁻¹. The full range of estimates is plotted in **Fig. 2b**, and is consistent
 221 with inferences of \dot{p}_M based on seafloor deflection.

222

223 **3. Results**

224 The co-evolution of $\Delta \sigma_{xx}$ and p_M over time is solved numerically through a forward Euler
 225 discretization of equation (2), with instantaneous stress changes prescribed when tectonic or

226 magmatic thresholds are reached (equations 4, 7 and 8). The corresponding codes are provided as
227 part of the Supplementary Material. Typical model behavior is illustrated in **Fig. 3**, which
228 represents 4 characteristic types of MOR section. **Fig. 3a** corresponds to a slow-spreading
229 segment with an 8-km thick axial lithosphere. It shows the continuous decrease of the diking
230 threshold from its peak (post-eruption) value of ~ 250 MPa, in response to increasing magma
231 pressure. For a new eruption to become possible, the diking threshold has to fall below the
232 faulting threshold (~ 63 MPa). Assuming a value of \dot{p}_M appropriate for this spreading rate (5×10^{-2}
233 Pa/s at $U = 2.5$ cm/yr according to our intermediate estimate, **Fig. 2b**), this occurs within ~ 130
234 years, which sets the characteristic recurrence time of magmatic intrusions. About 2 earthquakes
235 typically occur in 130 years, because far-field extension increases the axial stress fast enough to
236 overcome the characteristic earthquake stress drop twice in this time frame. Two out of three
237 “events” of seafloor spreading are thus tectonic. When averaged over time scales of kyr to tens
238 of kyr, this translates to an M value of 0.3. In **Fig. 3b**, the spreading and pressure rates are the
239 same, but on-axis lithospheric thickness is lowered to 3 km. This lowers both the diking and
240 faulting thresholds, as well as the difference between them. The recurrence time of eruptions is
241 thus reduced to ~ 50 years, which sometimes allows for an earthquake to occur, and sometimes
242 does not. The time-averaged M is consequently increased to 0.7. Similar mechanisms are at play
243 in **Fig. 3c**, which corresponds to a faster spreading rate, thinner lithosphere, and greater pressure
244 build-up rate. Finally, in **Fig. 3d**, the pressure rate is so fast that earthquakes cannot occur within
245 the short eruption recurrence time (~ 7 yrs). This leads to fully-magmatic seafloor spreading ($M =$
246 1).

247 To further explore the primary controls on M , we carried out 80000 simulations spanning a
248 wide range of pressure rates and spreading rates, with lithospheric thickness indexed on

249 spreading rate following the “thinnest” and “thickest” end-members introduced in **Fig. 2a**.
 250 Contour lines in **Fig. 4** shows the time-averaged M values yielded by each of these simulations.
 251 In **Fig. 2c**, we show the trends of M vs. spreading rate obtained upon combining the intermediate
 252 scenario for \dot{p}_M vs. spreading rate (solid curve in **Fig. 2b**, red lines in **Fig. 4**) with the two end-
 253 member scenarios for lithospheric thickness vs. spreading rate (red and blue curves in **Fig. 2a**).
 254 These two trends successfully bracket our dataset of M vs. spreading rate.

255

256 **4. Discussion**

257 4.1. Primary controls on M

258 The results shown in **Fig. 2** suggest that the non-linear increase in M with spreading rate may
 259 reflect both the (possibly linear) increase in the rate of magma pressure build-up (**Fig. 4**), and the
 260 change in lithospheric thickness, which is most pronounced at slow rates. The key effect of
 261 increasing lithospheric thickness is to increase the difference between the peak magmatic
 262 threshold stress $\Delta\sigma_{xx}^{M,MAX}$ and the tectonic threshold $\Delta\sigma_{xx}^F$ (**Fig. 3**). This in turn increases the
 263 characteristic recurrence time of magmatic intrusions, which can be approximated as:

$$264 \quad \tau_M = \frac{\Delta\sigma_{xx}^{M,MAX} - \Delta\sigma_{xx}^F}{p_M}. \quad (14)$$

265 This approximation is valid as long as an earthquake stress drop remains small compared to the
 266 difference between peak magmatic and tectonic thresholds. This ensures that an eruption closely
 267 follows the moment when $\Delta\sigma_{xx}^M$ becomes smaller than $\Delta\sigma_{xx}^F$. Once the timing of intrusions is
 268 known, an expression for M straightforwardly follows:

$$269 \quad M = \min\left(\frac{\delta_M}{U\tau_M}, 1\right). \quad (15)$$

270 The predictions from this analytical approximation closely match the values of M estimated from
271 our numerical simulations over a wide range of pressure and spreading rates (**Fig. 4**).

272 By combining the above equations with our linear model for \dot{p}_M vs. U (equation 13), we
273 can cancel out spreading rate from the expression of M (valid for $M < 1$), and obtain:

$$274 \quad M = \frac{\delta_M \frac{\partial \dot{p}_M}{\partial U}}{P_0 + \rho g \gamma H}, \quad (16)$$

275 where γ is a dimensionless factor introduced for concision: $\gamma = 1 - \mu'(1 - \lambda)$, with $\mu' =$
276 $\frac{\mu}{\mu + \sqrt{1 + \mu^2}}$. P_0 denotes a characteristic pressure: $P_0 = T_0 + p_w$, which is typically small (~ 10 MPa)

277 compared to the $\rho g \gamma H$ term (~ 100 MPa). Equation (16) is plotted in **Fig. 5a** for several values of
278 $\partial \dot{p}_M / \partial U$, which represent different scenarios for the increase in magma volume flux (expressed
279 as pressure increase in a shallow sill) with spreading rate. This graph clearly shows that a key
280 influence of spreading rate on M actually occurs through changes in lithospheric thickness H . In
281 fact, of all the parameters controlling M in our model, lithospheric thickness is the one that
282 changes most significantly from slow to fast spreading rates (**Fig. 2a**). The fact that using end-
283 member estimates of H vs. U appropriately brackets the available dataset of M vs. U (**Fig. 2c**)
284 further supports the idea that variability in lithospheric thickness is a strong source of variability
285 in M at MORs.

286 Bracketing the M dataset in **Fig. 2c** works best when using our intermediate estimate for
287 $\partial \dot{p}_M / \partial U$ (6.312×10^7 Pa.m⁻¹), which corresponds to the geometric average of high and low
288 estimates that span several orders of magnitude (Section 2.2.2, **Figs. 2b, 5b**). The value of
289 $\partial \dot{p}_M / \partial U$ depends on parameters such as crustal thickness and the number (N) and characteristic
290 cross-axis extent (w) of inflating sills (equation 13). These parameters are likely to vary
291 significantly from one ridge section to another, but may not show a systematic trend with respect

292 to spreading rate. Crustal thickness is for example known to remain roughly constant at ~6 km
293 for most MORs, except along ultraslow ridges where it can oscillate between ~0 and ~10 km
294 from segment to segment, because of extreme along-axis melt focusing (e.g., Dick et al., 2003;
295 Cannat et al., 2008; Sauter et al., 2011; Niu et al., 2015) (See Section 4.2). Unlike crustal
296 thickness, the cross-axis extent of shallow magma reservoirs is not well characterized.
297 Seismically-imaged AMLs generally appear narrower at faster ridges (e.g., Lowell et al., 2020),
298 but magma pressure may only build up in a small portion of the AML prior to an eruption
299 (Wilcock et al., 2009; Nooner and Chadwick, 2016), making w (of order $10^2 - 10^3$ m) difficult to
300 constrain. Finally, intrusion width δ_M is also a strong control on M in equation (16). Qin and
301 Buck (2008) pointed out that the typical width of dikes observed at ophiolites and MORs is ~1
302 m, and does not clearly correlate with spreading rate. These authors however noted that greater
303 tectonic stresses and a strong magmatic input could theoretically enable intrusions as wide as a
304 few meters.

305

306 4.2. Implications for seafloor spreading regimes

307 4.2.1. Symmetric vs. detachment faulting at slow spreading rates

308 Our model provides a straightforward explanation for the increased variability in M at slower
309 spreading rates (**Fig. 2c**) by directly attributing it to the increased variability in axial lithospheric
310 thickness (**Fig. 2a**). This variability is largely due to focusing of melt towards segment centers,
311 which makes the lithosphere warmer and thinner there compared to segment ends (Cannat,
312 1996). Variability in magma supply also occurs on a larger scale at slow and ultraslow MORs,
313 and shapes 50–100-km long MOR sections with axial volcanic ridges, symmetrically faulted
314 abyssal hill morphology ($M \sim 0.6-0.8$), and shallow seismicity. These sections alternate with

315 areas characterized by a more complex, "asymmetric" morphology associated with widespread
316 detachment faulting ($M \sim 0.2\text{--}0.6$), deeper and more active seismicity, deeper melt fractionation,
317 a greater occurrence of active hydrothermal sites, and in some extreme cases at ultraslow
318 spreading ridges: a much thinner or virtually absent igneous crust (Dick et al., 2003; Escartín et
319 al., 2008; Tucholke et al., 2008; Sauter et al., 2011; Olive and Escartín, 2016; Cannat et al.,
320 2019).

321 In our theoretical framework, M values of ~ 0.5 and below, which enable detachment
322 faulting (Buck et al., 2005), are a direct consequence of the lithosphere being locally thicker than
323 a threshold value of ~ 5 km (**Fig. 5a**; **Fig. 6**) for a given magmatic influx. This is fully consistent
324 with the fact that microseismicity appears confined within 5–6 km below seafloor at abyssal hill-
325 bearing sections of the Northern Mid-Atlantic Ridge, while detachment-bearing sections produce
326 micro-earthquakes down to ~ 12 km (e.g., Barclay et al., 2001; Parnell-Turner et al., 2017).
327 Detachment bearing sections may therefore receive an influx of melt comparable to
328 symmetrically-faulted sections, but allow a lesser fraction of this melt to intrude their colder,
329 thicker brittle lithosphere. The exact value of the threshold thickness for detachment faulting
330 however strongly depends on $\partial \dot{p}_M / \partial U$ (dashed green curve in **Fig. 5b**), which itself depends on
331 crustal thickness and a number of other poorly-constrained parameters. This could explain why
332 symmetrically faulted sections of ultraslow MORs such as Segment 27 of the Southwest Indian
333 Ridge can host micro-earthquakes ~ 10 km below seafloor (Yu et al., 2018). This segment is
334 indeed characterized by ~ 10 -km thick crust (Niu et al., 2015), a likely result of extreme along-
335 axis magma focusing (Dick et al., 2003). Such a high volume flux of magma could plausibly
336 cause anomalously high pressure build-up rates in magma reservoirs (compared to the global

337 trend of \dot{p}_M vs. spreading rate shown in **Fig. 2b**), which would enable M values in excess of 0.5
338 even in 10-km thick lithosphere (**Fig. 5**).

339 If for a given volume flux of magma, the time-averaged M is mainly set by lithospheric
340 thickness, it is important to keep in mind that lithospheric thickness itself is strongly controlled
341 by magmatic input. In a broad sense, the thermal structure of a MOR reflects a balance between
342 heat advected upwards from the asthenosphere —through magma ascent and mantle flow— and
343 heat transferred through the lithosphere by hydrothermal circulation (e.g., Chen and Morgan,
344 1990; Phipps-Morgan and Chen, 1993). Models that balance magmatic input and hydrothermal
345 output are generally successful at explaining the thermal state of MORs receiving a steady
346 magma supply, as they accurately replicate the depth to the shallowest AML at intermediate to
347 fast rates (**Fig. 2a**) (e.g., Phipps-Morgan and Chen, 1993). In these models, the heat input stems
348 from magmatic emplacement below the lithosphere (e.g., Maclennan et al., 2004), yet repeated
349 dike intrusions in the brittle domain are also likely to influence the equilibrium thermal structure
350 (e.g., Behn and Ito, 2008). Feedbacks are also likely to exist between hydrothermal and tectonic
351 processes. For example, fracturing associated with the damage zones of large-offset faults could
352 increase crustal permeability, and thus the vigor of hydrothermal convection in detachment-
353 bearing ridge sections (Escartín et al., 2008). Enhanced cooling would further thicken the
354 lithosphere, which in turn would promote lower M values that favor detachment faulting, in a
355 self-reinforcing feedback loop that would stabilize the detachment forming regime.

356

357 4.2.2. Transition to fully-magmatic spreading at faster spreading rates

358 Another important feature of our model is that it predicts conditions under which seafloor
359 spreading becomes fully magmatic ($M = 1$). This specifically occurs when axial lithosphere

360 becomes thinner than a critical thickness that is straightforwardly obtained by setting $M = 1$ in
361 equation (16), and strongly depends on $\partial \dot{p}_M / \partial U$ (**Fig. 5**). In the framework of Buck et al. (2005)
362 and Liu and Buck (2018; 2020), reaching $M = 1$ marks the transition between a mode of
363 spreading dominated by tectonic stretching, where M directly controls the characteristics of
364 faults that bound an axial valley (Behn and Ito, 2008; Olive et al., 2015), and a buoyancy-
365 dominated regime where an axial high forms due to the upward load exerted on the lithosphere
366 by low-density melts (**Fig. 6**). In this regime, only small inward- and outward-dipping faults
367 form to accommodate near-axis lithospheric flexure (e.g., Escartín et al., 2007). In real systems,
368 the transition from axial valley to axial rise occurs at intermediate rates, between 5.5 and 7.5
369 cm/yr (Dick et al., 2003), which corresponds to axial lithospheric thicknesses between ~ 2 and ~ 5
370 km (**Fig. 2a**). This is well accounted for by our model when using values $\partial \dot{p}_M / \partial U$ close to 10^8
371 Pa.m⁻¹ (**Fig. 5b**), which are well within the plausible range estimated in Section 2.2.2 and plotted
372 in **Fig. 2b**. This said, the extent to which the transition from axial valley to axial high truly
373 represents a transition to fully-magmatic spreading remains debatable. Ito and Behn (2008) for
374 example showed that alternating between periods of $M = 0$ and $M = 1$ lasting kyrs to tens of kyrs
375 could allow the growth of an axial high with a time-averaged $M < 1$, as is seen at some
376 intermediate and fast-spreading MORs. In numerical models, this requires the axis to be weak
377 enough to rapidly develop positive relief during intermittent, fully-magmatic phases.

378 A major transition in seafloor spreading modes was also observed in recent analog
379 experiments conducted by Sibrant et al. (2018) using Ludox. This viscous colloidal dispersion
380 behaves as an elastic-brittle material when mixed with salt. By pouring a saline solution from the
381 top down into a tank filled with Ludox, Sibrant et al. (2018) were able to model a brittle
382 lithosphere that diffusively thickens off-axis and overlies a fluid asthenosphere. Upon subjecting

383 this system to increasing extension rates, they observed a transition from fault-accommodated
384 plate separation to a regime dominated by vertical Ludox “intrusions”. They proposed that this
385 occurs when the axial thickness of the lithosphere (controlled by extension rate) falls below the
386 characteristic size of the process zone of mode-I cracks. They further showed that this reasoning
387 could be upscaled to real MORs to predict the switch to fully-magmatic extension at fast-
388 spreading rates. An interesting analogy can be drawn with our approach, in which intrusion-
389 dominated spreading occurs when (1) magma pressure builds up at a rapid rate in shallow
390 reservoirs and (2) axial lithosphere is thin enough that the difference between peak magmatic and
391 tectonic thresholds is low. Both of these conditions should be met at fast-spreading MORs. In the
392 experiments of Sibrant et al. (2018), it is unclear whether fluid pressure builds up at the base of
393 the lithosphere prior to intrusion events, and whether the rate of pressure increase is affected by
394 spreading rate. It may instead be controlled solely by the buoyancy difference between pure and
395 saline Ludox. If the pressure build-up rate is sufficiently fast, Ludox intrusions may become so
396 frequent that the differential stress required for faulting is never reached at the axis. In any case,
397 our respective modeling approaches agree that the transition to fully magmatic spreading
398 involves a threshold of axial lithospheric thickness (**Fig. 5b**; **Fig. 6**).

399

400 4.3. Model limitations and possible improvements

401 We have attempted to construct the simplest possible model that explains global trends of M vs.
402 spreading rate in terms of stress interactions between magmatic and tectonic events. By doing so,
403 we have made a number of simplifying assumptions that we briefly discuss here. First, we model
404 the seismic cycle as a time-predictable process (e.g., Shimazaki and Nakata, 1980) with a
405 constant stress build-up rate, triggering stress, and earthquake stress drop, all of which are likely

406 to fluctuate through time in a real system. In particular, we have only considered magnitude ~6
407 earthquakes, each accounting for 1 m of horizontal slip with total slip and 1 MPa of stress drop.
408 In reality, normal faulting earthquakes at MORs follow a Gutenberg-Richter distribution with
409 relatively high b-values (Olive and Escartín, 2016), which means that most of the seismically-
410 accommodated extension is accounted for by the largest earthquakes. The significant deficit of
411 MOR earthquakes compared to their expected moment release however suggests that a sizable
412 portion of tectonic extension may occur aseismically, particularly at faster-spreading ridges
413 (Cowie et al., 1993; Frohlich and Wetzel, 2007; Olive and Escartín, 2016). This idea is backed
414 up by recent numerical models of MOR seismic cycles (Mark et al., 2018).

415 Second, we rely on a simplified model for intrusion triggering which involves reaching the
416 tensile strength of the lithosphere at the roof of a magma pocket under the combined influence of
417 magmatic overpressure and tectonic stress. This is consistent with recent seismological
418 investigations of the early stage of an East Pacific Rise eruption, which began with synchronous
419 ruptures distributed over a distance spanning multiple distinct magma reservoirs (Tan et al.,
420 2016). This was interpreted as multiple, independently replenished AMLs —potentially out-of-
421 sync with respect to magma pressure— being brought to failure synchronously by tectonic
422 loading. Our model obviously does not capture the complexity of such events, warranting further
423 investigations of the 3-D stress field around replenishing sills (e.g., Wilcock et al., 2009;
424 Supplementary Fig. S1), and the consideration of alternative triggering criteria for example based
425 on fracture mechanics (e.g., Sibrant et al., 2018). Another limitation of our model is its
426 simplified treatment of magmatic pressure build-up, which we assume to occur at a constant,
427 poorly constrained rate, lumping together a number of complex processes related to sill
428 emplacement and replenishment in the lower oceanic crust. On the one hand, whether sill

429 replenishment happens continuously or in pulses depends on the way magma ascends to the base
430 of the lithosphere and through the axial mush zone, which could involve wave-like transport
431 (Parnell-Turner et al., 2020). On the other hand, the link between sill inflation rate and pressure
432 build-up potentially involves damping of pressure changes by viscous relaxation of hot rocks
433 above the magma (e.g., Kelemen and Aharonov, 1998) and poro-elastic effects in the
434 surrounding mush zone. Better characterizing the stress changes imparted by replenishing
435 magma reservoirs at MOR axes before and after intrusions will be key to improving our theory.
436 This will involve continuous monitoring of MOR axes through seafloor geodesy and seismology
437 (e.g., Nooner and Chadwick, 2016), with the caveat that extrapolating short-term measurements
438 to geological time scales will remain difficult until we at least capture a full seismic / volcanic
439 cycle, particularly at a slow ridge section not influenced by a hot spot (Tolstoy et al., 2001;
440 Dziak et al., 2004). Another difficulty in bridging time scales of seafloor spreading is the
441 increasing amount of evidence for temporal fluctuations in MOR activity on periods ranging
442 from 10s of kyrs to millions of years (e.g., Parnell-Turner et al., 2020). This has led Tolstoy
443 (2015) to question whether the behavior of MORs that we observe today is representative of past
444 or longer-term activity.

445 The last important limitation of our approach is the assumption that dikes and faults
446 compete to release the elastic strain energy stored in axial lithosphere, but have no possibility of
447 triggering each other. Such interactions have however been observed several times at rifts and
448 ridges. Calais et al. (2008) for example documented a 2007 slow slip event on a normal fault that
449 likely promoted the intrusion of a dike in the eastern branch of the East African Rift. Tolstoy et
450 al. (2001) reported the reciprocal phenomenon of a migrating dike triggering a dozen magnitude
451 ~5 earthquakes along the normal faults that bound the axial valley of the Gakkel ridge (85°N),

452 throughout most of the year 1999. This raises the question of whether tectonic extension at
453 MORs primarily occurs during or in response to magmatic events. We note that the 20+ km
454 length of the valley-bounding faults at Gakkel makes them susceptible to nucleating magnitude
455 ~6–6.5 earthquakes (Wells and Coppersmith, 1994). Such events could occur separately from
456 intrusions and would account for ~3 times more slip over the same along-axis distance compared
457 to ~10 magnitude-5 earthquakes. Again, a longer record of observations is needed to assess
458 whether the tectonic extension that accompanies dike intrusion is systematically small compared to the
459 associated magmatic extension, and/or to purely tectonic spreading events. Dziak et al (2004) for
460 example estimated that all the seismicity associated with the 2001 dike intrusion event at the
461 Lucky Strike segment of the Mid-Atlantic Ridge amounted to centimeters of horizontal
462 extension, which would be negligible if the dike alone accommodated ~1 m of extension. In any
463 case, available observations warrant the development of more detailed seismic cycle models of
464 MOR faults (e.g., Mark et al., 2018) that interact with an inflating sill and episodic dike
465 intrusions. This will require detailed constraints on the geometry of the fault(s) relative to that of
466 the magmatic plumbing system, as static stress transfers often display sharp spatial variations
467 (Supplementary Figure S1). The modes of volcano-tectonic or tectono-volcanic triggering may
468 thus be strongly dependent on the local geometry of the ridge, e.g., a deeper magmatic system at
469 a slower MOR would influence faults within a broader horizontal area compared to a shallow
470 sill-dike system at a fast MOR (e.g., Tolstoy et al., 2001).

471

472 **5. Conclusions**

473 We have designed a simple theoretical framework explaining the long-term partitioning of
474 magmatic and tectonic extension at MORs in terms of short-term cycles of earthquakes and dike

475 intrusions that interact with one another by modulating the stress state of the ridge axis (**Figs. 1,**
476 **3**). Axial lithospheric thickness and the rate of pressure build-up in shallow, replenishing magma
477 sills are the two main parameters controlling M in our model (**Fig. 4**). We constructed plausible
478 scenarios for the increase of pressure rate with spreading rate, as well as end-member trends for
479 lithospheric thickness across MOR spreading rates (**Fig. 2a, b**). This allowed us to bracket the
480 observed non-linear increase in M and relate its reduced variability with increasing spreading
481 rate (**Fig. 2c**) to reduced along-axis variability in lithosphere thickness.

482 To first-order, spreading rate controls the flux of magma that reaches the ridge axis. The
483 thermal component of this flux fuels hydrothermal circulation, which modulates the strength and
484 thickness of axial lithosphere. The mass component of this flux contributes to setting the pace of
485 pressure build-up in shallow sills, which together with lithosphere thickness, sets the value of M .
486 This in turn controls the intensity of tectonic deformation, which could affect the vigor of
487 hydrothermal circulation through pervasive fracturing of the crust, exerting a feedback on
488 lithosphere thickness. The dichotomy between symmetrically faulted and detachment-bearing
489 sections of slow MORs could thus reflect thresholds in lithosphere thickness under a near
490 constant along-axis magma flux (**Figs. 5 & 6**). Extreme focusing of melt along the axis of
491 ultraslow MORs however points to the combined action of a spatially-varying magma flux and
492 lithosphere thickness in shaping symmetrically-faulted segments and quasi-amagmatic sections.
493 On the other end of the spectrum, the large, spatially uniform influx of magma to fast MORs
494 ensures a uniformly thin lithosphere with frequent intrusions, which makes fully magmatic
495 spreading possible. Overall, modes of seafloor spreading reflect a balance between magmatic,
496 tectonic, and hydrothermal processes, raising the question of whether temporal fluctuations in
497 magma supply can alter the stability of these equilibria and trigger regime transitions.

498

499 **Acknowledgements**

500 We wish to thank our editor Jean-Philippe Avouac as well as Maya Tolstoy and an anonymous
501 reviewer for their helpful feedback. This work greatly benefited from discussions with Mark
502 Behn, Roger Buck, Mathilde Cannat, Javier Escartín and Garrett Ito. J.-A.O. was supported by
503 an Emergence(s) - Ville de Paris grant, and NSF grant OCE-1654745. This work relied
504 exclusively on previously published data. All the codes necessary to reproduce our results are
505 provided as part of the Supplementary Material, and are available at
506 <https://github.com/jaolive/TectoMagMOR>.

507

508

509

510 **Appendix A.**

511 Supplementary Material related to this article consists of:

- 512 • Supplementary Information (.pdf file). Additional details regarding the modeling of seafloor
513 inflation at the East Pacific Rise to infer pressure increase rates in a shallow magma reservoir.
514 Instructions on how to use the supplementary codes. This file includes 4 Supplementary Figures.
- 515 • Supplementary Code: M_across_rates.m; a MATLAB script producing Figs. 1a, 2, 3, 4 and 5.
- 516 • Supplementary Code: tectono_magmatic_fcn.m; MATLAB implementation of the toy model of
517 tectono-volcanic cycles.
- 518 • Supplementary Text files: .txt files for use by the MATLAB scripts, containing datasets of M
519 (M_data.txt), micro-earthquake depths (depth_of_microEQs.txt), and AML depths
520 (depth_of_AMLs.txt).

521 **References**

- 522 Barclay, A.H., Toomey, D.R., Solomon, S.C., 2001. Microearthquake characteristics and crustal
523 V_p/V_s structure at the Mid-Atlantic Ridge, 35°N, *Journal of Geophysical Research*, 106,
524 2017-2034.
- 525 Behn, M.D., Ito, G., 2008. Magmatic and tectonic extension at mid-ocean ridges: 1. Controls on
526 fault characteristics. *Geochemistry, Geophysics, Geosystems*, 9.
527 doi:10.1029/2008GC001965.
- 528 Bickert, M., Lavier, L., Cannat, M., 2020. How do detachment faults form at ultraslow mid-
529 ocean ridges in a thick axial lithosphere? *Earth and Planetary Science Letters*, 533.
530 doi:10.1016/j.epsl.2019.116048.
- 531 Buck, W.R., Carbotte, S., Mutter, C.Z., 1997. Controls on extrusion at mid-ocean ridges,
532 *Geology*, 25, 935-938.
- 533 Buck, W.R., Lavier, L., Poliakov, A.N.B., 2005. Modes of faulting at mid-ocean ridges. *Nature*,
534 434, 719–723. doi: 10.1038/nature03358.
- 535 Calais, E., d'Oreye, N., Albaric, J., Deschamps, A., Delvaux, D., Déverchère, J., Ebinger, C.,
536 Ferdinand, R.W., Kervyn, F., Macheyek, A.S., Oyen, A., Perrot, J., Saria, E., Smets, B.,
537 Stamps, D.S., Wauthier, C., 2008. Strain accommodation by slow slip and dyking in a
538 youthful continental rift, East Africa. *Nature*, 456. doi:10.1038/nature07478.
- 539 Cannat, M., 1996. How thick is the magmatic crust at slow spreading oceanic ridges? *Journal of*
540 *Geophysical Research*, 101(B2), 2847-2857.
- 541 Cannat, M., Sauter, D., Bezos, A., Meyzen, C., Humler, E., Le Rigoleur, M., 2008. Spreading
542 rate, spreading obliquity, and melt supply at the ultraslow spreading Southwest Indian Ridge.
543 *Geochemistry, Geophysics, Geosystems*, 9(4). doi:10.1029/2007GC001676.

544 Cannat, M., Sauter, D., Lavier, L., Bickert, M., Momoh, E., Leroy, S., 2019. On spreading modes
545 and magma supply at slow and ultraslow mid-ocean ridges. *Earth and Planetary Science*
546 *Letters*, 519, 223-233. doi:10.1016/j.epsl.2019.05.012.

547 Chen, Y., Morgan, W.J., 1990. A nonlinear rheology model for mid-ocean ridge axis topography.
548 *Journal of Geophysical Research*, 95(B11), doi:10.1029/JB095iB11p17583.

549 Cowie, P.A., Scholz, C.H., Edwards, M., Malinverno, A., 1993. Fault strain and seismic coupling
550 on mid-ocean ridges. *Journal of Geophysical Research*, 98(B10), 17,911-17,920.

551 Dick, H.J.B., Lin, J., Schouten, H., 2003. An ultraslow-spreading class of ocean ridge. *Nature*,
552 426.

553 Dziak, R.P., Smith, D.K., Bohnenstiehl, D.R., Fox, C.J., Desbruyeres, D., Matsumoto, H.,
554 Tolstoy, M., Fornari, D.J., 2004. Evidence of a recent magma dike intrusion at the slow
555 spreading Lucky Strike segment, Mid-Atlantic Ridge. *Journal of Geophysical Research*, 109,
556 doi:10.1029/2004JB003141.

557 Escartín, J., Cowie, P.A., Searle, R.C., Allerton, S., Mitchell, N.C., MacLeod, C.J., Slootweg,
558 A.P., 1999. Quantifying tectonic strain and magmatic accretion at a slow spreading ridge
559 segment, Mid-Atlantic Ridge, 29°N. *Journal of Geophysical Research*, 104, 10421-10437.
560 <https://doi.org/10.1029/1998JB900097>.

561 Escartín, J., Soule, S.A., Fornari, D.J., Tivey, M., Schouten, H., Perfit, M., 2007. Interplay
562 between faults and lava flows in construction of the upper oceanic crust: The East Pacific
563 Rise crest 9°25'-58'N. *Geochemistry, Geophysics, Geosystems*, 8 (Q06005).

564 Escartín, J., Smith, D.K., Cann, J.R., Schouten, H., Langmuir, C.H., Escrig, S., 2008. Central
565 role of detachment faults in accretion of slow-spreading oceanic lithosphere. *Nature*, 455,
566 7214, 790–794. doi: 10.1038/nature07333.

567 Frohlich, C., Wetzel, L.R., 2007. Comparison of seismic moment release rates along different
568 types of plate boundaries, *Geophysical Journal International*, 171, 909-920.

569 Gillis, K.M., 2008. The roof of an axial magma chamber: a hornfelsic heat exchanger, *Geology*,
570 36, 299–302.

571 Grevemeyer, I., Hayman, N.W., Lange, D., Peirce, C., Papenberg, C., Van Avendonk, H.J.A.,
572 Schmid, F., Gómez de La Peña, L., Dannowski, A., 2019. Constraining the maximum depth
573 of brittle deformation at slow- and ultraslow-spreading ridges using microseismicity.
574 *Geology*, 47(11), 1069-1073. doi:10.1130/G46577.1.

575 Heap, M.J., Villeneuve, M., Albino, F., Farquharson, J.I., Brothelande, E., Amelung, F., Got, J.-
576 L., Baud, P., 2020. Towards more realistic values of elastic moduli for volcano modelling. *J.*
577 *Volc. Geotherm. Res.*, 390. doi:10.1016/j.jvolgeores.2019.106684.

578 Howell, S., Ito, G., Behn, M.D., Martinez, F., Olive, J.-A., Escartín, J., 2016. Magmatic and
579 tectonic extension at the Chile Ridge: Evidence for mantle controls on ridge
580 segmentation. *Geochemistry, Geophysics, Geosystems*, 17. doi:10.1002/2016GC006380.

581 Howell, S., Olive, J.-A., Ito, G., Behn, M.D., Escartín, J., Kaus, B., 2019. Seafloor expression of
582 oceanic detachment faulting reflects gradients in mid-ocean ridge magma supply. *Earth and*
583 *Planetary Science Letters*, 516.

584 Ito, G., Behn, M.D., 2008. Magmatic and tectonic extension at mid-ocean ridges: 2. Origin of
585 axial morphology. *Geochemistry, Geophysics, Geosystems*, 9(Q08O10).

586 Kappel, E.S., Ryan, W.B.F., 1986. Volcanic episodicity and a non-steady rift valley along
587 Northeast Pacific spreading centers: Evidence from Sea MARC I. *Journal of Geophysical*
588 *Research*, 91(B14), 13925-13940.

589 Kelemen, P., Aharonov, E., 1998. Periodic formation of magma fractures and generation of
590 layered gabbros in the lower crust beneath oceanic spreading ridges, in *Faulting and*
591 *Magmatism at Mid-Ocean Ridge*, Geophysical Monograph Series, 106, Buck, W.R. et al.
592 (editors), AGU, Washington, D.C. doi:10.1029/GM106p0291.

593 Keller, T., May, D.A., Kaus, B.J.P., 2013. Numerical modelling of magma dynamics coupled to
594 tectonic deformation of lithosphere and crust. *Geophysical Journal International*, 195(3),
595 1406-1442.

596 Liu, Z., Buck, W.R., 2018. Magmatic controls on axial relief and faulting at mid-ocean ridges.
597 *Earth and Planetary Science Letters*, 491. doi:10.1016/j.epsl.2018.03.045.

598 Liu, Z., Buck, W.R., 2020. Global trends of axial relief and faulting at plate spreading centers
599 imply discrete magmatic events. *Journal of Geophysical Research*,
600 doi:10.1029/2020JB019465.

601 Lowell, R.P., Zhang, L., Maqueda, M.A.M., Banyte, D., Tong, V.C.H., Johnston, R.E.R., Harris,
602 R.N., Hobbs, R.W., Peirce, C., Robinson, A.H., Kolandaivelu, K., 2020. Magma-
603 hydrothermal interactions at the Costa Rica Rift from data collected in 1994 and 2015. *Earth*
604 *and Planetary Science Letters*, 531.

605 Macdonald, K.C., Fox, P.J., Alexander, R.T., Pockalny, R., Gente, P., 1996. Volcanic growth
606 faults and the origin of Pacific abyssal hills. *Nature*, 380, 125-129.

607 Maclennan, J., Hulme, T., Singh, S.C., 2004. Thermal models of oceanic crustal accretion:
608 Linking geophysical, geological, and petrological observations. *Geochemistry, Geophysics,*
609 *Geosystems*, 5(2).

610 MacLeod, C.J., Searle, R.C., Murton, B.J., Casey, J.F., Mallows, C., Unsworth, S.C., Achenbach,
611 K.L., Harris, M., 2009. Life cycle of oceanic core complexes. *Earth and Planetary Science*

612 Letters, 287, 333-344.

613 Mark, H.F., Behn, M.D., Olive, J.-A., Liu, Y., 2018. Controls on mid-ocean ridge normal fault
614 seismicity across spreading rates from rate-and-state friction models. *Journal of Geophysical*
615 *Research*, 123.

616 Niu, X., Ruan, A., Li, J., Minshull, T.A., Sauter, D., Wu, Z., Qiu, X., Zhao, M., Chen, Y.J.,
617 Singh, S., 2015. Along-axis variation in crustal thickness at the ultraslow spreading
618 Southwest Indian Ridge (50°E) from a wide-angle seismic experiment. *Geochemistry,*
619 *Geophysics, Geosystems*, 16, 468-485, doi:10.1002/2014GC005645.

620 Nooner, S.L., Webb, S.C., Buck, W.R., Cormier, M.-H., 2014. Post eruption inflation of the East
621 Pacific Rise at 9°50'N. *Geochemistry, Geophysics, Geosystems*, 15, 2676-2688.
622 doi:10.1002/2014GC005389.

623 Nooner, S.L., Chadwick, W.W., 2016. Inflation-predictable behavior and co-eruption
624 deformation at Axial Seamount. *Science*, 354(6318), 1399-1403.
625 doi:10.1126/science.aah4666.

626 Olive, J.-A., Behn, M.D., Tucholke, B.E., 2010. The structure of oceanic core complexes
627 controlled by the depth-distribution of magma emplacement. *Nature Geoscience*, 3., 491–
628 495, doi:10.1038/ngeo888.

629 Olive, J.-A., Behn, M.D., Ito, G., Buck, W.R., Escartín, J., Howell, S., 2015. Sensitivity of
630 seafloor bathymetry to climate-driven fluctuations in mid-ocean ridge magma
631 supply. *Science*, 350(6258).

632 Olive, J.-A., Escartín, J., 2016. Dependence of seismic coupling on normal fault style along the
633 Northern Mid-Atlantic Ridge. *Geochemistry, Geophysics, Geosystems*, 17.

634 Parnell-Turner, R., Sohn, R.A., Peirce, C., Reston, T.J., MacLeod, C.J., Searle, R.C., Simão,
635 N.M., 2017. Oceanic detachment faults generate compression in extension. *Geology*, 45(10),
636 923-926. doi:10.1130/G39232.1.

637 Parnell-Turner, R., Sim, S.J., Olive, J.A., 2020. Time-dependent crustal accretion on the
638 Southeast Indian Ridge revealed by Malaysia Airlines MH370 search, *Geophysical Research*
639 *Letters*, doi:10.1029/2020GL087349.

640 Phipps Morgan, J., Chen, Y.J., 1993. The genesis of oceanic crust: Magma injection,
641 hydrothermal circulation, and crustal flow. *Journal of Geophysical Research*, 98(B4), 6283-
642 6297. doi:10.1029/92JB02650.

643 Qin, R., Buck, W.R., 2008. Why meter-wide dikes at spreading centers? *Earth and Planetary*
644 *Science Letters*, 265, 466-474.

645 Rubin, A.M., 1995a. Propagation of magma-filled cracks. *Annual Review of Earth and Planetary*
646 *Sciences*, 23, 287-336.

647 Sauter, D., Cannat, M., Rouméjon, S., Andréani, M., Birot, D., Bronner, A., Brunelli, D., Carlut,
648 J., Delacour, A., Guyader, V., Macleod, C.J., Manatschal, G., Mendel, V., Ménez, B., Pasini,
649 V., Ruellan, E., Searle, R.C., 2013. Continuous exhumation of mantle-derived rocks at the
650 Southwest Indian Ridge for 11 million years. *Nature Geoscience*, 6, 314–320.

651 Schouten, H., Smith, D.K., Cann, J.R., Escartín, J., 2010. Tectonic versus magmatic extension in
652 the presence of core complexes at slow-spreading ridges from a visualization of faulted
653 seafloor topography. *Geology*, 38(7), 615–618. doi: 10.1130/G30803.1.

654 Shimazaki, K., Nakata, T., 1980. Time-predictable recurrence model for large earthquakes.
655 *Geophysical Research Letters*, 7(4), 279-282.

656 Sibrant, A.L.R., Mittelstaedt, E., Davaille, A., Pauchard, L., Aubertin, A., Auffray, L., Pidoux,

657 R., 2018. Accretion mode of oceanic ridges governed by axial mechanical strength. *Nature*
658 *Geoscience*, 11, 274-279. doi:10.1038/s41561-018-0084-x.

659 Singh, S.C., Crawford, W.C., Carton, H., Seher, T., Combier, V., Cannat, M., Canales, J.P.,
660 Düsünür, D., Escartín, J., Miranda, J.M., 2006. Discovery of a magma chamber and faults
661 beneath a Mid-Atlantic Ridge hydrothermal field. *Nature*, 442. doi:10.1038/nature05105.

662 Sinton, J.M., and Detrick, R.S., 1992. Mid-ocean ridge magma chambers. *Journal of Geophysical*
663 *Research*, 97, 197-216. doi:10.1029/91JB02508.

664 Solomon, S.C., Huang, P.Y., Meinke, L., 1988. The seismic moment budget of slowly spreading
665 ridges. *Nature*, 334, 58–60.

666 Tan, Y.J., Tolstoy, M., Waldhauser, F., Wilcock, W.S.D., 2016. Dynamics of a seafloor
667 spreading episode at the East Pacific Rise. *Nature*, 540, 261-265.

668 Tian, X., Choi, E., 2017. Effects of axially variable diking rates on faulting at slow spreading
669 mid-ocean ridges. *Earth and Planetary Science Letters*, 458, 14–21.

670 Tolstoy, M., Bohnenstiehl, D.R., Edwards, M.H., Kurras, G.J., 2001. Seismic character of
671 volcanic activity at the ultraslow-spreading Gakkel ridge. *Geology*, 29, 1139–1142.

672 Tolstoy, M., 2015. Mid-ocean ridge eruptions as a climate valve. *Geophysical Research Letters*,
673 42, 1346–1351.

674 Tucholke, B.E., Behn, M.D., Buck, W.R., Lin, J., 2008. Role of melt supply in oceanic
675 detachment faulting and formation of megamullions. *Geology*, 36, 455-458.

676 Wells, D.L., Coppersmith, K.J., 1994. New empirical relationships among magnitude, rupture
677 length, rupture width, rupture area and surface displacement. *Bulletin of the Seismological*
678 *Society of America*, 84, 974–1002.

679 Wilcock, W.S.D., Hooft, E.E., Toomey, D.R., McGill, P.R., Barclay, A.H., Stakes, D.S.,

680 Ramirez, T.J., 2009. The role of magma injection in localizing black-smoker activity. *Nature*
681 *Geoscience*, 2, 509-513.

682 Yu, Z., Li, J., Niu, X., Rawlinson, N., Ruan, A., Wang, W., Hu, H., Wei, X., Zhang, J., Liang,
683 Y., 2018. Lithospheric structure and tectonic processes constrained by microearthquake
684 activity at the central ultraslow-spreading Southwest Indian Ridge (49.2° to 50.8°E). *Journal*
685 *of Geophysical Research*, 123, 6247-6262.

686 **Figure 1 – a.** Fraction of magmatic extension across spreading rates. MAR: Mid-Atlantic Ridge;
687 GSC: Galapagos Spreading Center; JdF: Juan de Fuca Ridge; CR: Chile Ridge; SEIR: Southeast
688 Indian Ridge; ELSC: Eastern Lau Spreading Center; EPR: East Pacific Rise. Data from Cowie et
689 al. (1993); Ito and Behn (2008); Olive and Escartín (2016) and Howell et al. (2016). **b.** Model
690 setup.

691
692 **Figure 2 – a.** Estimates of axial lithospheric thickness from seismically imaged AML depths
693 (circles, as compiled by Buck et al., 1997; Singh et al., 2006) and depth of micro-earthquakes
694 (squares, as compiled by Grevemeyer et al., 2019). Colored lines correspond to thick and thin
695 end-members as defined by equation (10). Light-green stars correspond to example cases shown
696 in Fig. 3. Sd: Slow, detachment faulting regime; Ss: Slow, symmetric faulting regime; I:
697 Intermediate; F: Fast. **b.** Modeled pressure rate vs. spreading rate (equation 13), with
698 intermediate estimate as continuous line and high and low estimates as dashed lines. Estimates
699 from seafloor deflection at the EPR (See Supplementary Material) are shown as vertical bars
700 (Mo: Mogi; La: Laccolith models). **c.** Same dataset of M vs. U as in Fig. 1, with curves
701 corresponding to the thin (red) and thick (blue) end-members models.

702
703 **Figure 3 –** Modeled tectono-volcanic cycles (axial stress $\Delta\sigma_{xx}$, in black, and diking threshold
704 $\Delta\sigma_{xx}^M$, in red, vs. time) in 4 example configurations. **a.** slow, detachment-bearing ridge section
705 (Sd in Fig. 2): $H = 8$ km; $U = 2.5$ cm/yr. **b.** slow, symmetrically faulted ridge section (Ss): $H = 3$
706 km; $U = 2.5$ cm/yr. **c.** Intermediate-spreading MOR (I): $H = 2.5$ km; $U = 6$ cm/yr. **d.** Fast-
707 spreading MOR (F): $H = 1.5$ km; $U = 15$ cm/yr. In each example the pressure rate is 3.1560×10^7
708 $\text{Pa} \cdot \text{m}^{-1} \cdot \text{s}^{-2}$ times the spreading rate (intermediate estimate) from Fig. 2b.

709

710 **Figure 4** – Model predictions of M as a function of spreading rate and magma pressure rate. The
711 color code corresponds to the analytical approximation from equations (14) and (15) while black
712 contour lines (spanning $M = 0.1$ to 1, with increments of 0.1) show results from the simulations.
713 The red line is the average estimate of pressure rate vs. U , and the dashed red line is the high
714 estimate. Panels a and b respectively correspond to the thin and thick lithosphere end-members
715 of H vs. U shown in Fig. 2a.

716

717 **Figure 5 – a.** Lithospheric thickness control on M for different values of $\partial \dot{p}_M / \partial U$ corresponding
718 to the vertical bars in panel b. The solid curves correspond to the low (blue), intermediate (black)
719 and high (red) estimates of pressure rate vs. spreading rate from Fig. 2b. **b.** Green dashed curve:
720 critical lithospheric thickness above which extension becomes detachment-dominated ($M = 0.5$,
721 dashed green circle in panel a), plotted against $\partial \dot{p}_M / \partial U$. Green solid curve: critical lithospheric
722 thickness below which extension becomes fully magmatic ($M = 1$, solid green circle in panel a).
723 These critical thicknesses are obtained by setting $M = 0.5$ or 1 in equation (16).

724

725 **Figure 6** – Schematic diagram of major seafloor spreading modes as a function of spreading rate
726 and axial lithosphere thickness. Vertical orange arrow represents volume flux of magma to
727 shallowest reservoir (orange ellipse), which is assumed to scale linearly with spreading rate.
728 Horizontal dashed lines represent lithosphere thickness thresholds identified in Fig. 5. Each
729 spreading mode corresponds to a case shown in Fig. 3: Sd: Slow, detachment faulting regime;
730 Ss: Slow, symmetric faulting regime; I: Intermediate; F: Fast.

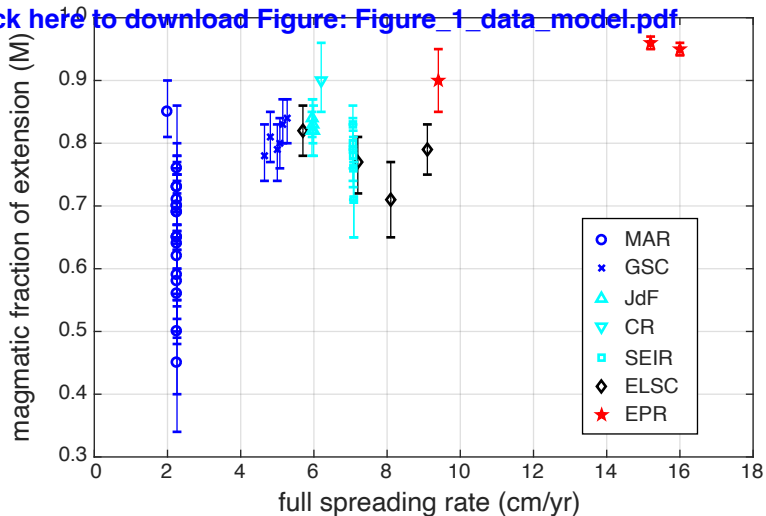
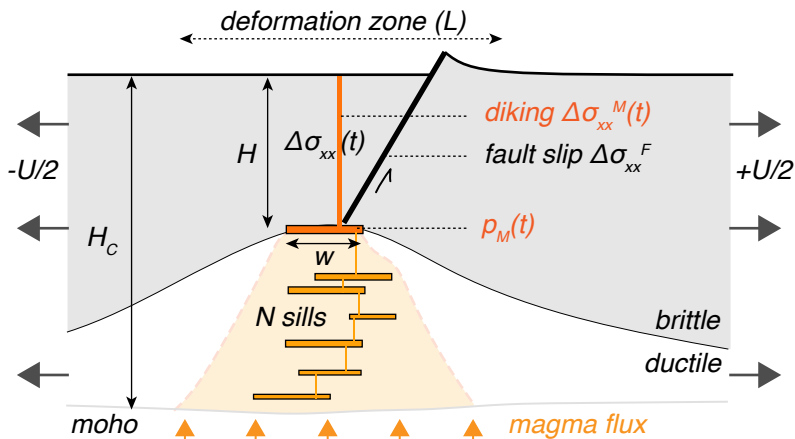
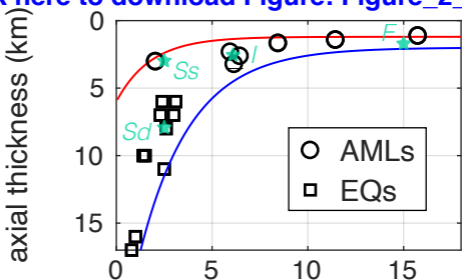
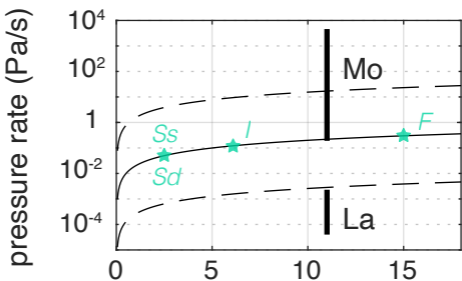
Figure 1[Click here to download Figure: Figure_1_data_model.pdf](#)**b.**

Figure 2

[Click here to download Figure: Figure_2_M...](#)



b.



c.

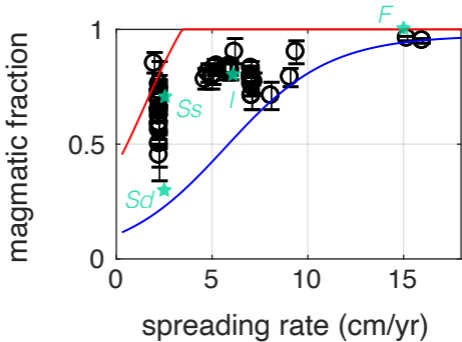


Figure 3
[Click here to download Figure: Figure_3_cycles.pdf](#)

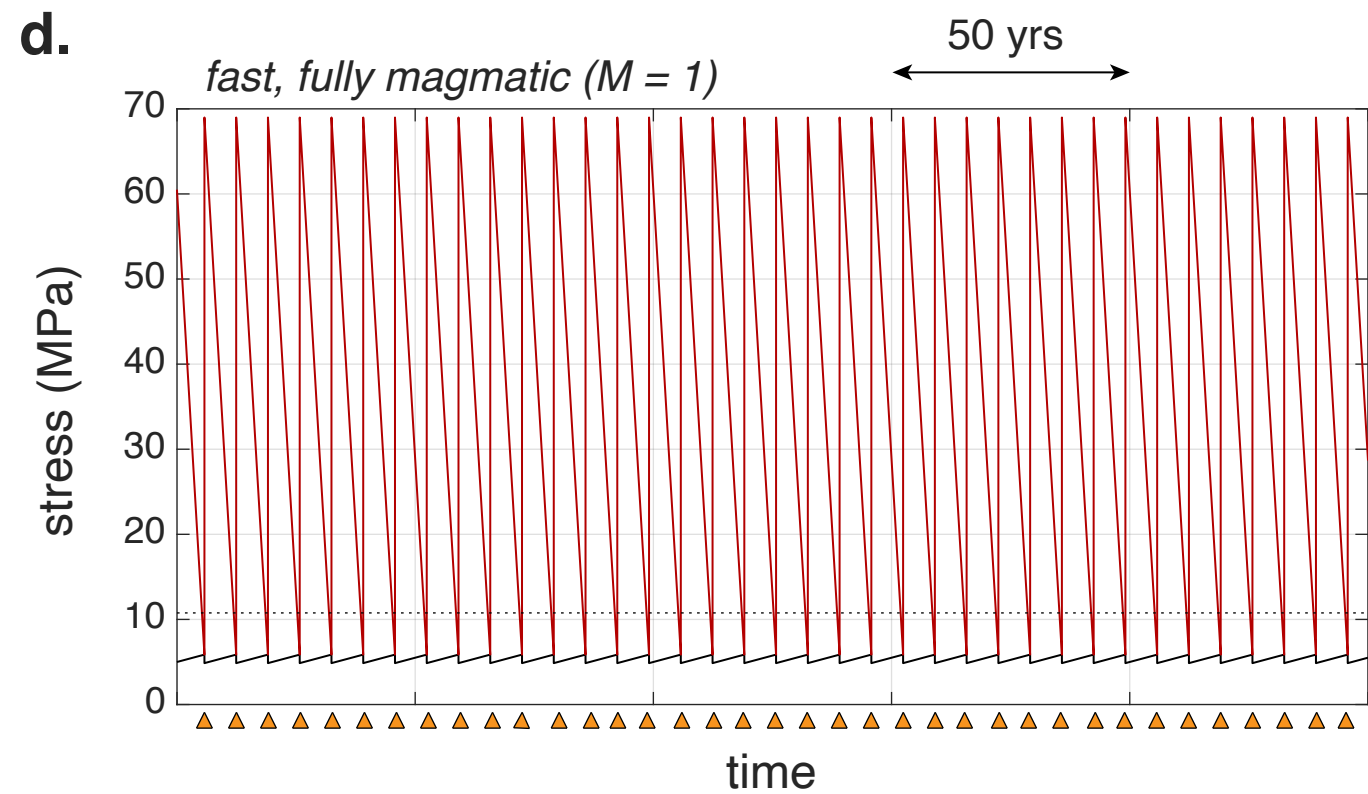
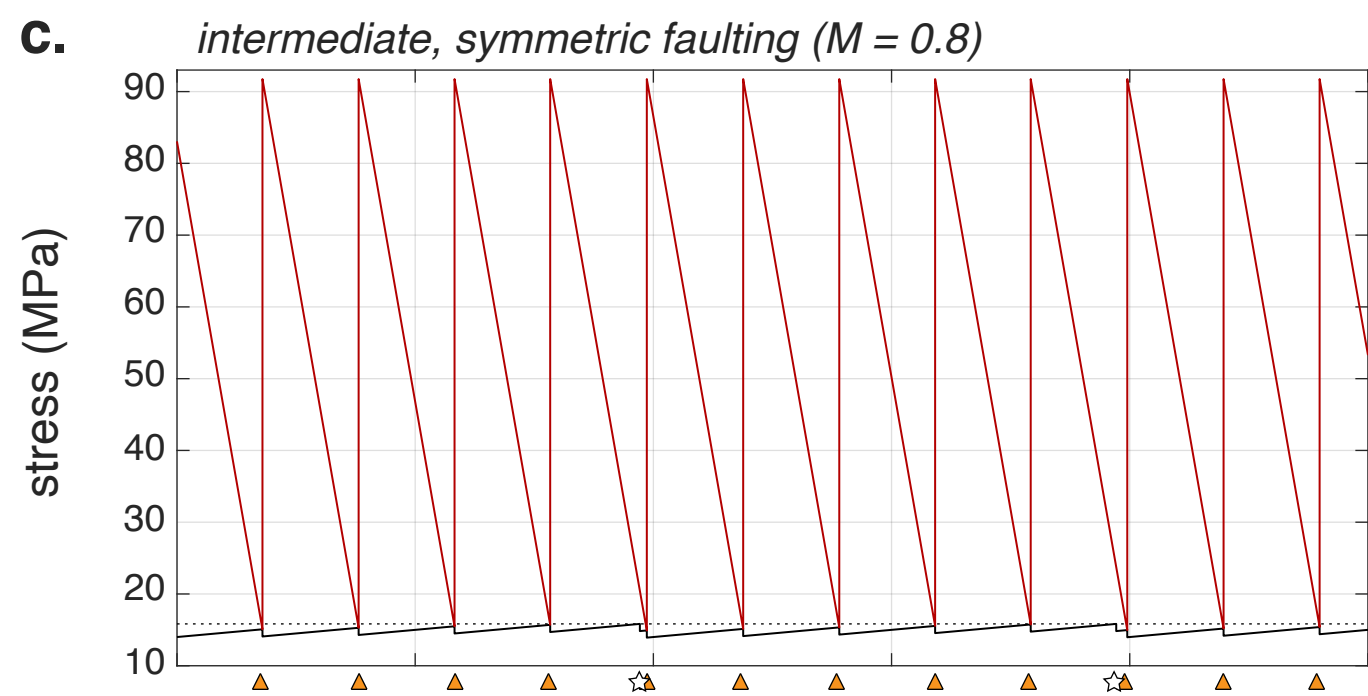
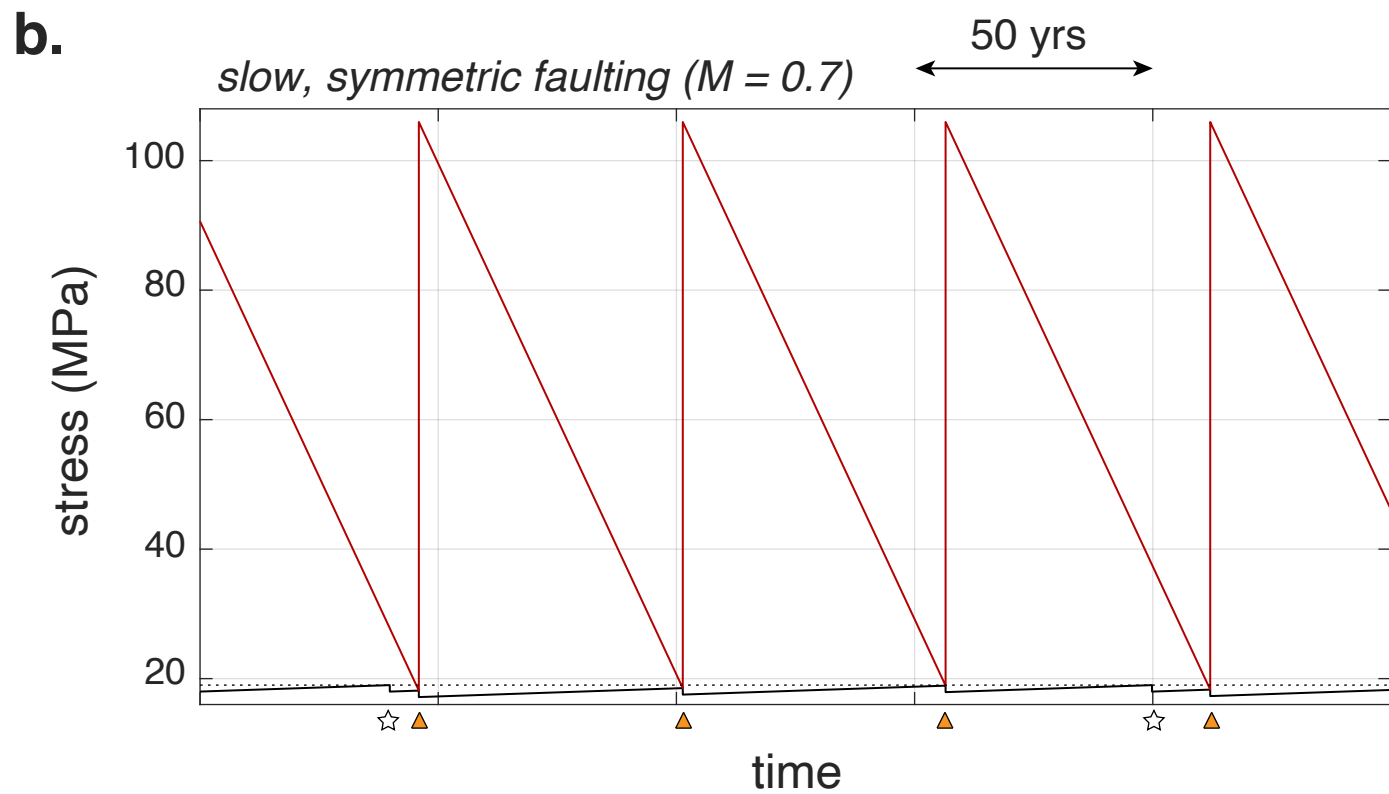
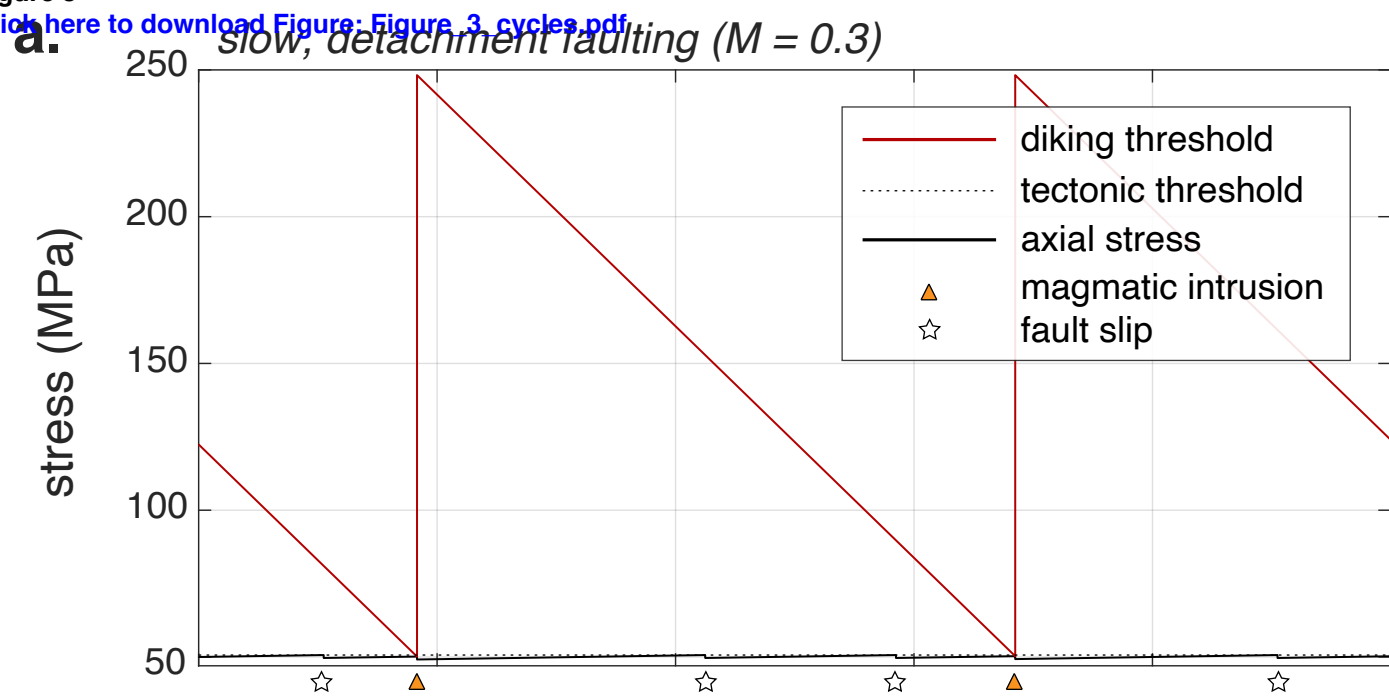


Figure 4
[Click here to download Figure: Figure_4_M_maps.pdf](#)

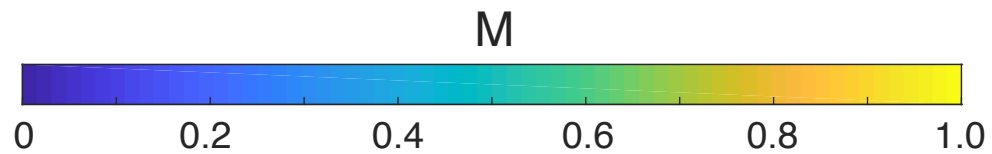
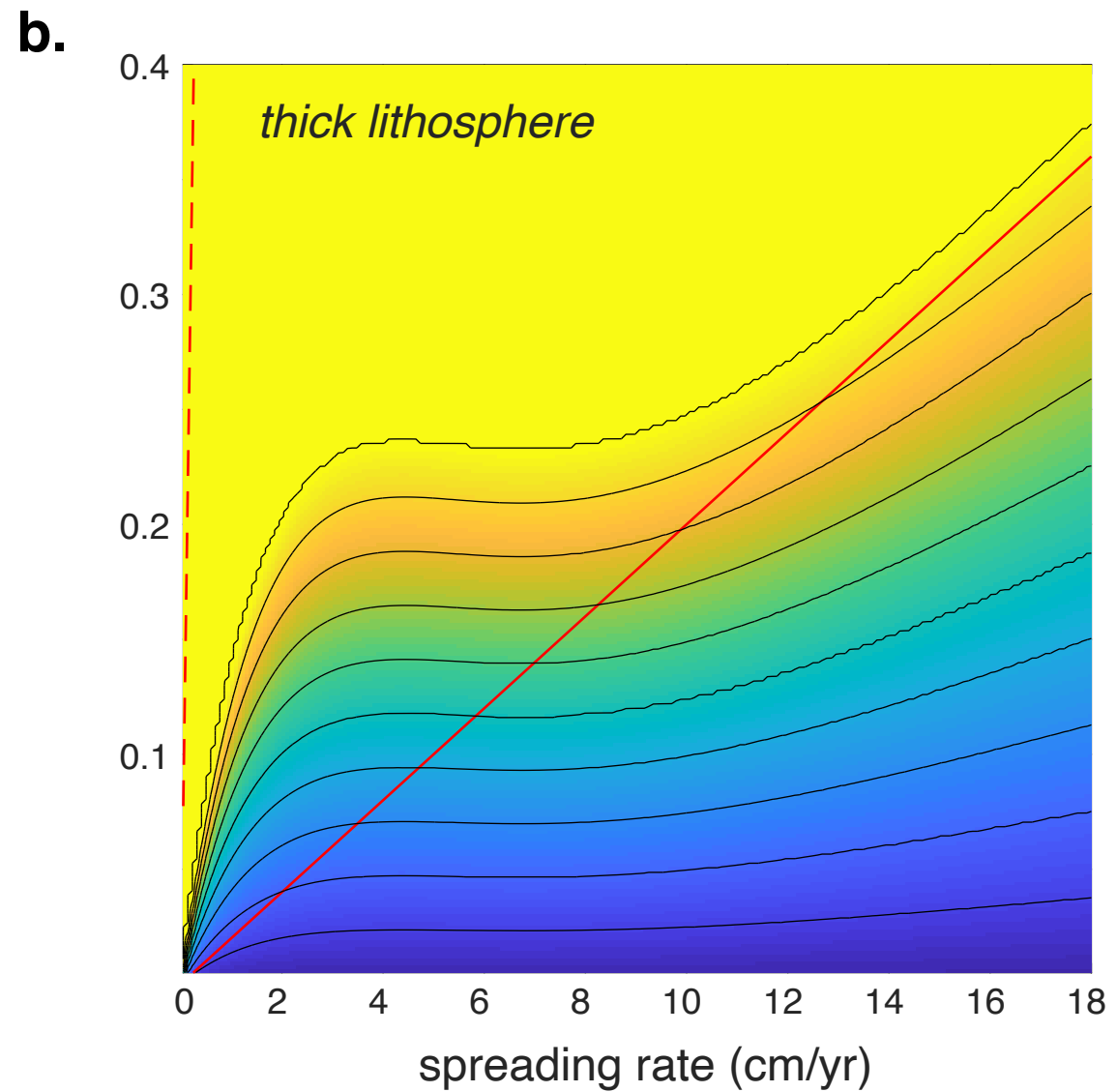
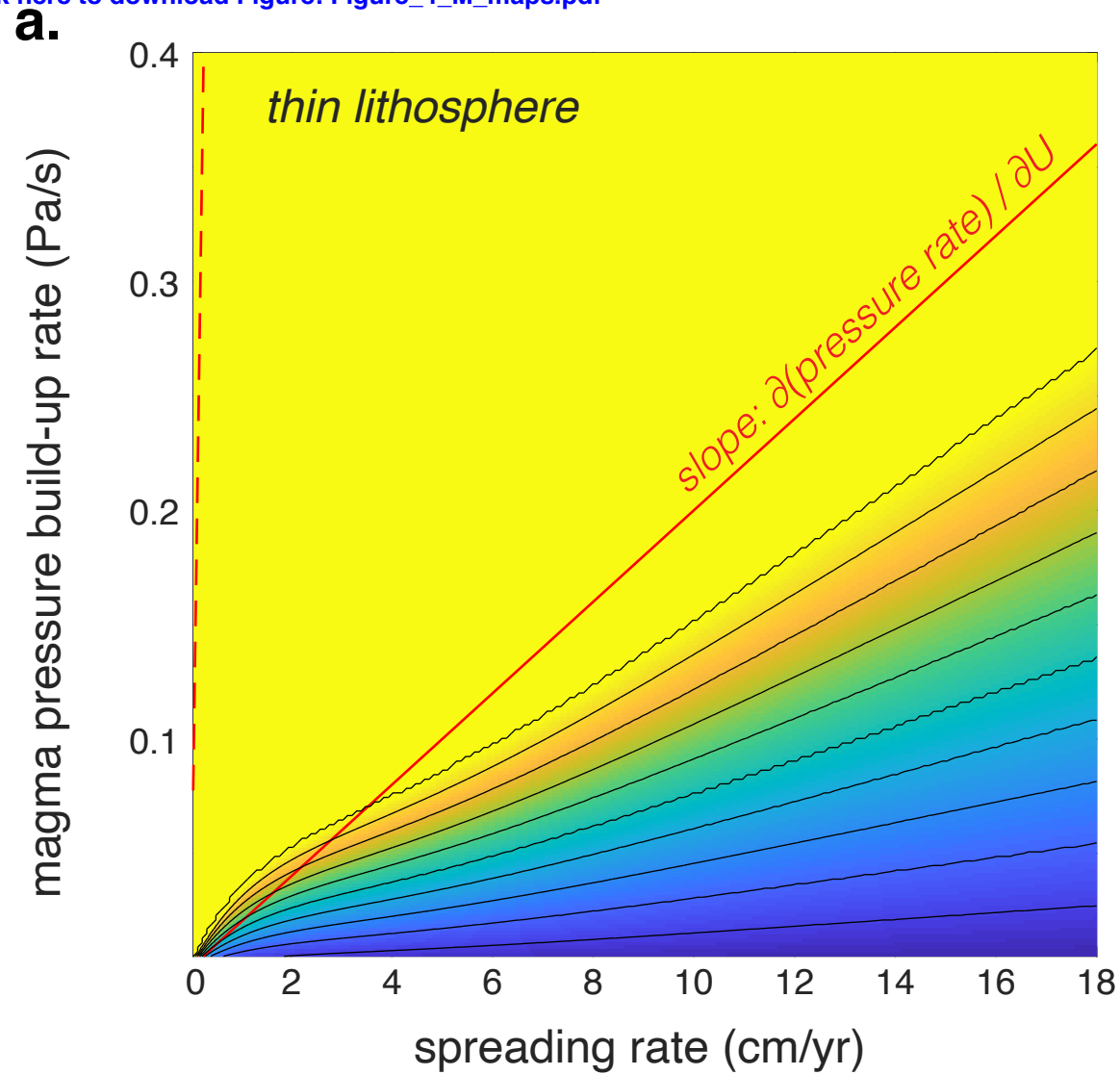


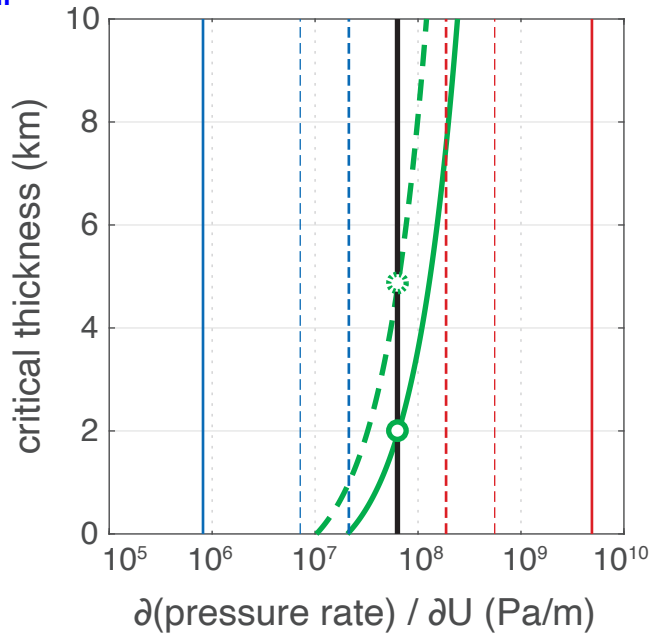
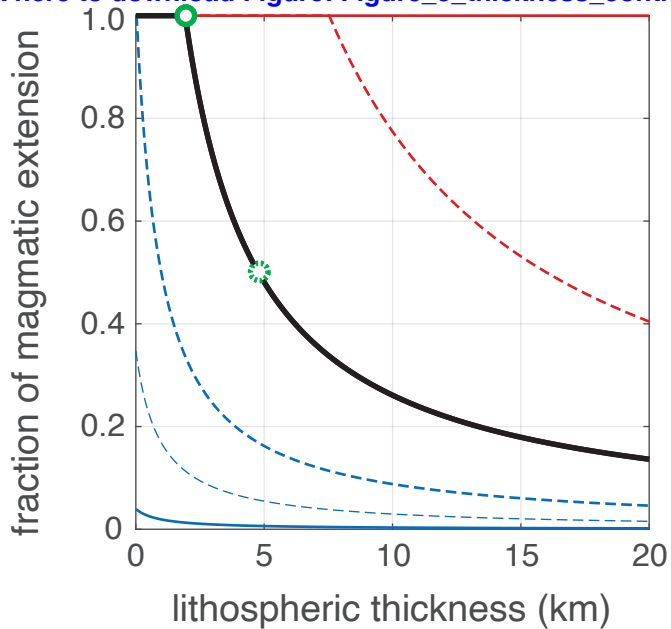
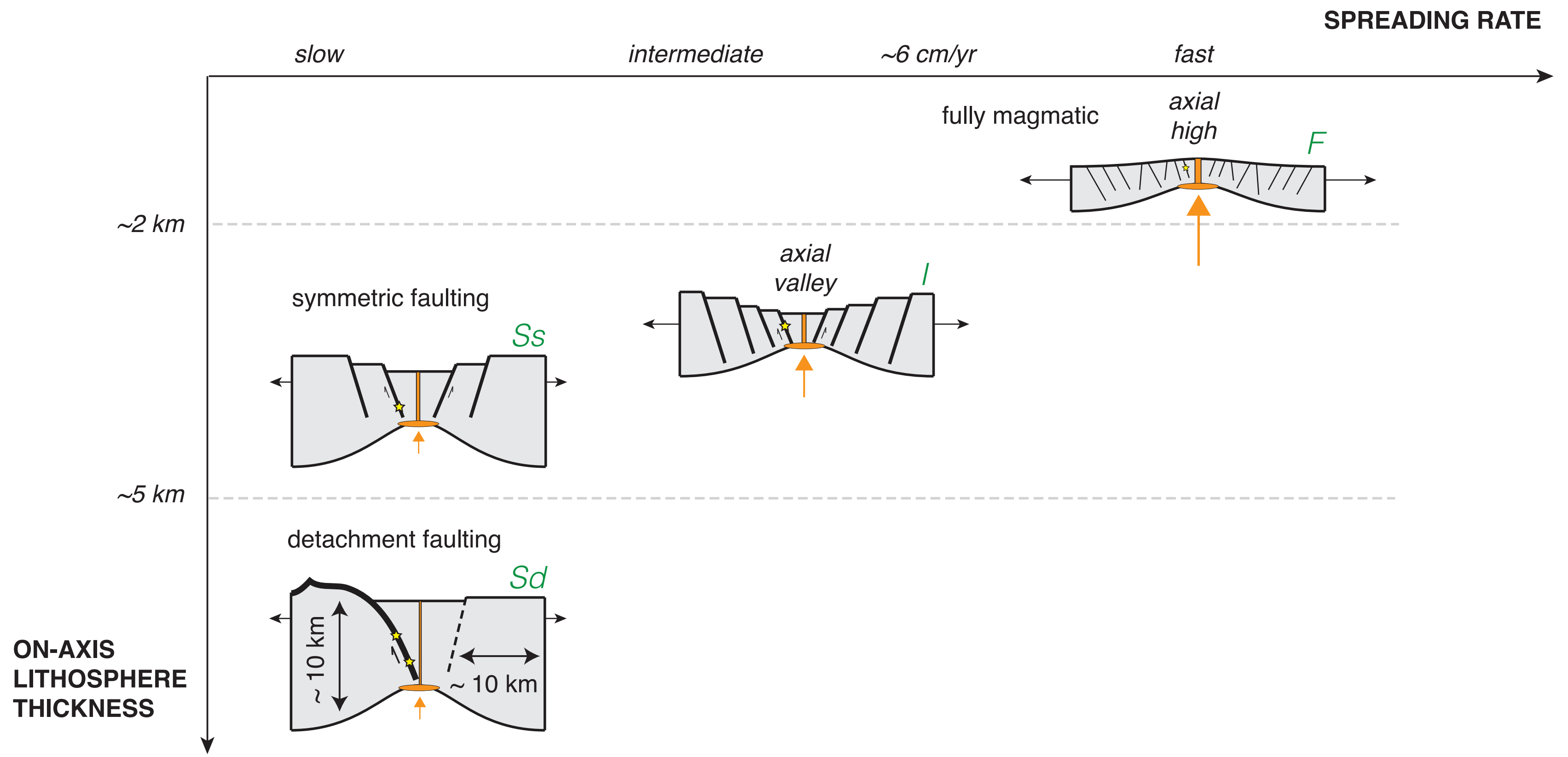
Figure 5[Click here to download Figure: Figure_5_thickness_control.pdf](#)

Figure 6

[Click here to download Figure: Figure_6_summary_cartoon.pdf](#)



Supplementary Information for ”Controls on the magmatic fraction of extension at mid-ocean ridges”

Jean-Arthur Olive ¹and Pierre Dublanchet ²

¹Laboratoire de Géologie, École Normales Supérieure / CNRS UMR 8538, PSL Research University, Paris 75005, France

²MINES ParisTech, PSL Research University, Centre de Géosciences, 35 rue saint-honoré 77305 Fontainebleau, France

Contents of this file

1. Text S1
2. Text S2
3. Figures S1 to S4

Text S1: Magmatic pressure rates at the East Pacific Rise

Here we provide two different estimates of the magmatic pressure rate characterizing the inflation of a shallow melt lens at the axis of a mid-ocean ridge. We specifically rely on the seafloor uplift rates recorded by Nooner, Webb, Buck, and Cormier (2014), and fit the measurements with two end-member models of magma reservoir.

Corresponding author: J.-A. Olive, Laboratoire de Géologie, École Normale Supérieure / CNRS UMR 8538, PSL Research University, Paris 75005, France (olive@geologie.ens.fr)

The first one is a Mogi point source within an elastic half-space (Mogi, 1958). In this case, the surface vertical displacement rates v are given by:

$$v(r) = \frac{(1 - \nu)V_0}{\pi} \frac{d}{(r^2 + d^2)^{3/2}}, \quad (1)$$

where d is the depth of the source, r is the radial distance from the source at the seafloor, ν is the Poisson's ratio of the elastic half-space and V_0 an equivalent volumetric flux, defined as:

$$V_0 = \frac{\pi \dot{p}_m a^3}{G}, \quad (2)$$

\dot{p}_m , a and G being the magmatic pressure rate, the source radius and the shear modulus of the elastic medium respectively. Here, the Poisson's ratio ν is considered constant $\nu = 0.25$ and we invert for the depth d and the volumetric flux V_0 using a grid search algorithm. Confidence intervals on d and V_0 are presented in figure S2a., and the comparison between acceptable models and the data are shown in figure S2b. V_0 ranges from 1.2×10^6 to $4.8 \times 10^6 \text{ m}^3.\text{yr}^{-1}$ at the 60% confidence level (figure S2a.). End-member values for the source radius ($a = 50 \text{ m}$ and $a = 500 \text{ m}$) and the shear modulus ($G = 2 \text{ GPa}$ and $G = 12 \text{ GPa}$, Heap et al. (2020)) lead to plausible pressure rates \dot{p}_m ranging from 1.9×10^{-1} to $4.6 \times 10^3 \text{ Pa.s}^{-1}$.

We then inverted the same dataset using the laccolith model of (Turcotte & Schubert, 2002). In this setup, the lithosphere is treated as a thin elastic plate of rigidity D uplifted above a magma reservoir (of full width L and overpressure p_m). The surface vertical displacement are given by:

$$v(r) = \begin{cases} \frac{\dot{p}_m}{24D} \left(r^4 - \frac{L^2 r^2}{2} + \frac{L^4}{16} \right) & \text{if } r \leq L/2 \\ 0 & \text{if } r > L/2 \end{cases} \quad (3)$$

D is given by:

$$D = \frac{EH^3}{1 - \nu^2}, \quad (4)$$

where E , ν and H are the Young's modulus, the Poisson's ratio and the thickness of the elastic plate. The Poisson's ratio and the thickness are considered fixed here at $\nu = 0.25$ and $H = 1.5$ km (Fig. 2a, see main text). We invert for the magmatic pressure rate \dot{p}_m and the laccolith width L assuming two extreme scenarios for the Young's modulus ($E = 5$ GPa and $E = 30$ GPa, corresponding to $G = 2$ GPa and $G = 12$ GPa, Heap et al. (2020)). Results are shown in figures S3 ($E = 5$ GPa) and S4 ($E = 30$ GPa). To the 60% confidence level, \dot{p}_m ranges from 4.0×10^{-5} to 2.3×10^{-3} Pa.s⁻¹.

Text S2: Reproducing results and figures with supplementary codes

We provide supplementary codes to fully reproduce the results and figures from the main text. MATLAB script *M_across_rates.m* plots the analytical model, and uses function *tectono_magmatic_fcn.m* to run toy model simulations. To generate Figs. 1b; 2; 3; 4 and 5, one can run *M_across_rates.m* by setting variable *regime* (line 9) to 'thin' or 'thick' to select an end-member scenario for lithospheric thickness vs. spreading rate (red and blue curves in Fig. 2a). All scripts must be run from the same folder, which must include the three .txt files containing the M (*M_data.txt*), micro-earthquake depth (*depth_of_microEQs.txt*), and AML depth (*depth_of_AMLs.txt*) datasets, respectively.

References

- Heap, M. J., Villeneuve, M., Albino, F., Farquharson, J. I., Brothelande, E., Amelung, F., ... Baud, P. (2020). Towards more realistic values of elastic moduli for volcano modelling. *Journal of Volcanology and Geothermal Research*, *390*, 106684.
- Mogi, K. (1958). Relations between the eruptions of various volcanoes and the deformations of the ground surfaces around them. *Earthq Res Inst*, *36*, 99–134.
- Nooner, S. L., Webb, S. C., Buck, W. R., & Cormier, M.-H. (2014). Post eruption inflation of the east pacific rise at 9 50 n. *Geochemistry, Geophysics, Geosystems*, *15*(6), 2676–2688.
- Pollard, D. D., & Segall, P. (1987). Theoretical displacements and stresses near fractures in rock: with applications to faults, joints, veins, dikes, and solution surfaces. In B. K. Atkinson (Ed.), *Fracture mechanics of rock* (p. 277 - 349). London: Academic Press.
- Turcotte, D. L., & Schubert, G. (2002). *Geodynamics*. Cambridge university press.

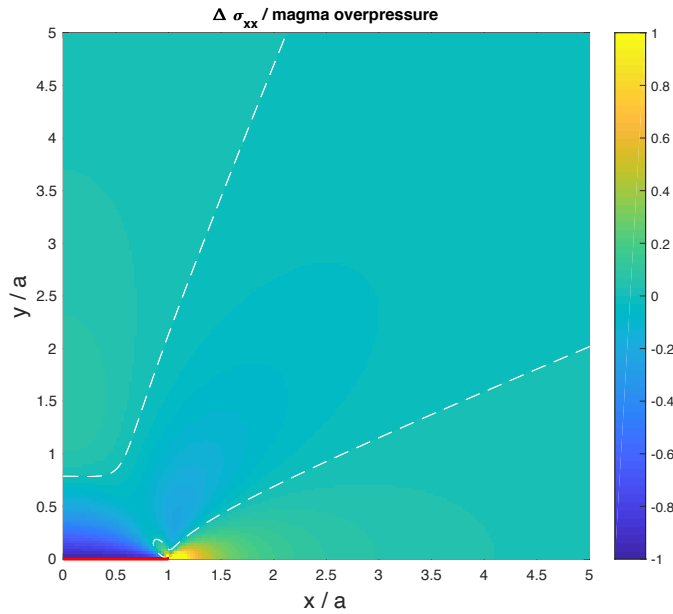


Figure S1. Change in total horizontal stress induced by an over-pressured sill of half-width a (red line), normalized by overpressure (Pollard & Segall, 1987). Yellow lobes show areas where tensile stress builds up and a dike is likely to initiate. Tensile stress perturbation in this region is of same order of magnitude as magmatic overpressure. White dashed lines show contours of zero stress perturbation.

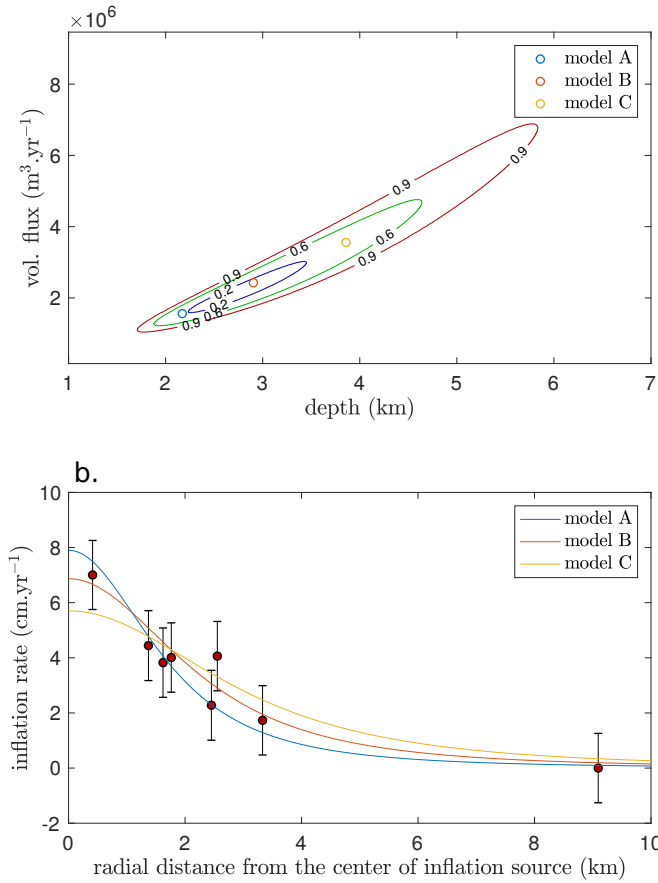


Figure S2. a. Source depths and volumetric fluxes explaining seafloor vertical displacements at the East Pacific Rise following the model of Mogi (1958). Labels on the contours indicate the confidence level. Colored dots indicate the parameters used for the model predictions shown in b. b. Data (red dots) vs. model predictions (colored lines) of equation (1).

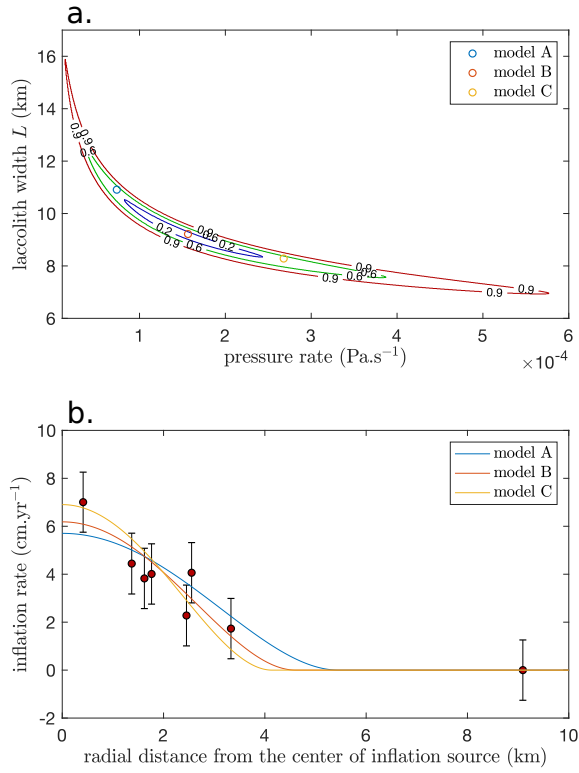


Figure S3. Same figure as figure S2 for the laccolith model of equation (3), assuming $G = 2$ GPa.

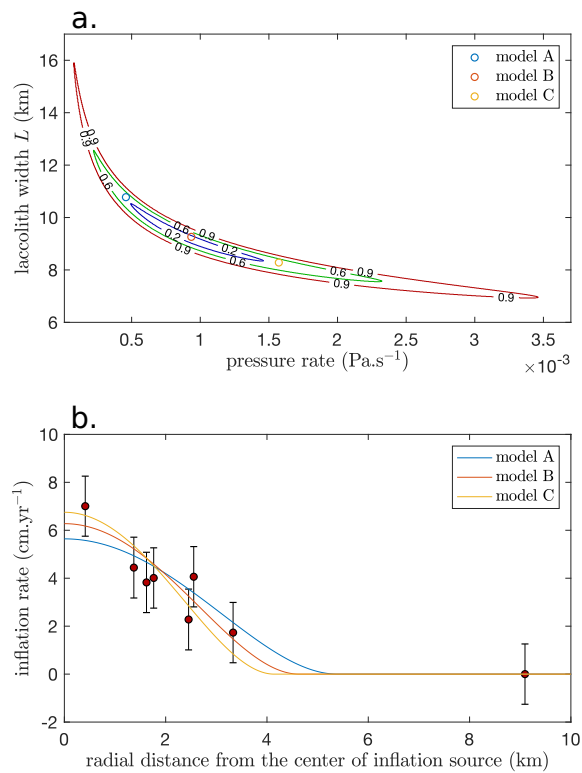


Figure S4. Same figure as figure S2 for the laccolith model of equation (3), assuming $G = 12$ GPa.